Available online at www.sciencedirect.com
ScienceDirect
Comput. Methods Appl. Mech. Engrg. 361 (2020) 112754
Computer methods in applied mechanics and engineering
www.elsevier.com/locate/cma

Application of PHT-splines in bending and vibration analysis of cracked Kirchhoff–Love plates

Javier Videla[a,c], Felipe Contreras[a], Hoang X. Nguyen[b], Elena Atroshchenko[a,c,*]

[a] Department of Mechanical Engineering, University of Chile, Santiago 8370448, Chile
[b] Department of Mechanical and Construction Engineering, Northumbria University, Newcastle upon Tyne NE1 8ST, United Kingdom
[c] University of New South Wales, School of Civil and Environmental Engineering, Sydney, Australia

Received 16 February 2019; received in revised form 9 August 2019; accepted 11 November 2019
Available online 29 November 2019

Abstract

In this work, we present an eXtended Geometry Independent Field approximaTion (X–GIFT) formulation for cracked Kirchhoff–Love plates. The plate geometry is modeled by Non-Uniform Rational B-Splines (NURBS) while the solution is approximated by Polynomial Splines over Hierarchical T-meshes (PHT-splines) and enriched by the Heaviside function and crack tip asymptotic expansions. The adaptive refinement is driven by a recovery-based error estimator. The formulation is employed for bending and vibration analysis. We compare different strategies for refinement, enrichment and evaluation of fracture parameters. The obtained results are shown to be in a good agreement with the reference solutions.

Keywords: Kirchhoff–Love plate theory; Fracture mechanics; Extended isogeometric analysis; Recovery-based error estimates; PHT-splines; Adaptive refinement

1. Introduction

Plate elements have found their applications in broad areas of engineering analysis from structural slabs in houses and buildings to aircraft's wings. The most commonly used model to predict the behaviors of plates is derived from the Kirchhoff–Love theory [1] as it requires only three degree of freedoms (DOF) of displacement without including rotation unknowns. The fundamental assumption of this theory is that the transverse shear deformations are neglected. This means if a cross-section is normal to the midplane of the plate before deformation, it remains normal to the midplane after deformation. For this reason, the transverse shear stresses are neglected while the in-plane ones remain accountable. Therefore, Kirchhoff–Love theory is applicable for thin plates in which the aspect ratio between the length and thickness is large. It is worth noting that the Kirchhoff–Love theory results in a fourth-order problem which requires C^1-continuity of the basis function if a numerical approach is involved to solve for approximate solutions. While this requirement causes a challenging issue for traditional finite element method with Lagrange basis function, such higher-order formulation can be handled efficiently by means of isogeometric analysis (IGA).

* Corresponding author at: Department of Mechanical Engineering, University of Chile, Santiago 8370448, Chile.
E-mail address: e.atroshchenko@unsw.edu.au (E. Atroshchenko).

https://doi.org/10.1016/j.cma.2019.112754
0045-7825/

1.1. Isogeometric analysis

The IGA approach was introduced by Hughes and co-workers [2] with the aim to bridge the gap between the computer-aided design (CAD) system and the analysis, or normally referred as computer-aided engineering (CAE) in the commercial sector. To achieve this seamless integration, the same basis functions are used to represent the geometry in CAD and to approximate the unknown fields. There are many possibilities for such basis function including B-splines, non-uniform rational B-splines (NURBS), T-splines, and polynomial splines over hierarchical T-meshes (PHT-splines). While all those functions preserve the exact geometry and are highly smooth, i.e., easily handle the high order approximations, B-splines and NURBS suffer from the drawback of tensor product which makes a purely local refinement fundamentally challenging. Meanwhile, T-splines were initially proposed by Sedeberg et al. [3] with ability to facilitate adaptivity. Their integration in the IGA framework is presented in the work of Bazilevs et al. [4], Dörfel et al. [5] which are followed by the development of analysis suitable T-splines by Scott et al. [6,7]. However, as pointed out in the work of Buffa et al. [8], the linear independence of the basis functions is not guaranteed for generic T-meshes. Nguyen-Thanh et al. [9] initially proposed the use of PHT-splines, which was introduced by Deng et al. [10], in the IGA framework for two-dimensional elastic solids. This approach has been proved to possess desirable features including smooth functions, geometrical flexibility, and local refinement. There has been much progress in the implementation and development of hierarchical T-splines, Nguyen-Thanh and Zhou [11] worked on the application of an extended formulation for crack propagation, Anitescu et al. [12] proposed a recovery-based error estimator for high order splines over T-meshes, while Chen and de Borst [13] proposed an extension of T-splines to local refinement within the Bézier extraction framework.

1.2. Geometry Independent Field approximaTion (GIFT)

The Geometry Independent Field approximaTion (GIFT) initially introduced by Marussing et al. [14] in the context of Boundary Element Method (BEM) and then generalized in the work of Atroshchenko et al. [15], consists in allowing different spaces for the parameterization of the computational domain and the approximation of the solution field. In particular, it allows to preserve the exactness of the CAD geometry, while using a more suitable and flexible set of basis functions for the solution field. The main features of GIFT are:

1. Preserving exact CAD geometry provided in any form, including B-splines or NURBS, at any stage of the solution process.
2. Allowing local refinement of the solution by choosing appropriate field approximations, independent from the geometrical parameterization of the domain.
3. Allowing computational savings by not refining the geometry during the process of refining the solution and by choosing simpler approaches for the solution, that is, using polynomial functions instead of rational functions.

GIFT has been applied to problems of heat transfer (Poisson's equation) and linear elasticity [15], yielding optimal convergence rates, even for pairs of geometry and field bases that do not pass the patch-test. Recently, Anitescu et al. [12] employed the GIFT idea in a high-order PHT-splines formulation for problems of 2D and 3D elasticity and adaptive refinement. Peng et al. [16] employed the GIFT formulation to study adaptive refinement for frequency analysis in vibration of Reissner–Mindlin plates. Note, that the formulation, developed in [16], is not locking-free. Shear-locking phenomena can be addressed by developing approximation spaces for the displacements and rotations, that satisfy the Kirchhoff constrain at the limit of thickness tending to zero [17].

Application of GIFT for time harmonic acoustics is given in the work of Videla et al. [18]. In the present work, we will pair NURBS geometries with a PHT-splines solution basis to model fracture mechanics problems under the Kirchhoff–Love plate theory. This choice will allow us to improve the numerical solution by employing local adaptive refinement near the crack tip and crack faces, while preserving the geometry exactness.

1.3. A posteriori error estimator

A specific criterion needs to be defined to drive adaptivity, usually an error estimator. As an *a posteriori* error estimator is used for evaluating the true error and guiding mesh refinement, it needs to be reliable at both local and

global level. The majority of the error estimator can be categorized into two types, namely, the residual-based error estimators and recovery-based error estimator (or error estimators using recovery techniques). The residual type of error estimator was initially proposed by Babuška and Rheinboldt [19]. This error estimator is computed by using the residual of the finite element solution, as the approximate solution from the numerical method does not satisfy the governing partial differential equations. Meanwhile, Zienkiewicz and Zhu first introduced the recovery type of error estimator with further development by considering superconvergent path recovery [20,21]. For this case, a recovered and more accurate solution of a quantity, normally stresses, is calculated in the post-processing stage based on the finite element solution. The error is then defined as the difference between the recovered solution and the finite element one. As the framework is straightforward, this type of error estimator is easy to implement. In addition, it is computationally inexpensive because of the involvement of the post-process quantity only, without having to solve the system of equations multiple times. These beneficial features made the recovered-based error estimator widely applied in engineering [22]. In [18] a comparison between residual-based and recovery-based error estimators was recently done in the context of the Helmholtz equation, leading in both cases to similar results. In this work, we propose a recovery-based error estimator based on the stress definition in the framework of the Kirchhoff–Love theory.

1.4. Fracture analysis for plates

Regarding the fracture analysis, there has been a well-established body of work on the investigation of structures with cracks using numerical tools including the well-known extended finite element method (XFEM) [23]. The main idea of this method is that the approximation functions are enriched across the crack faces and near the crack tip to represent the discontinuity and asymptotic behavior of the solution. Consequently, the mesh does not need to comply with the crack geometry, which simplifies the meshing procedure. The same enrichment idea of the XFEM has been applied to several methods, such as extended isogeometric analysis (X–IGA) [24–26], isogeometric boundary element [27], isogeometric-meshfree [28], and recently to X–IGA based on T-splines [29], X–IGA based on Bézier extraction operator [30], and PHT-Splines [11]. Although all the previous formulations have been proved to be effective to tackle 2D and 3D fracture mechanic problems, there is not the same amount of literature regarding their applications in plates.

Application of the XFEM and its variations has already been done to different plate theories. Dolbow et al. [31] initially proposed an XFEM formulation applied to Reissner–Mindlin plates, Xing et al. [32] employed a new set of high-order crack tip enrichment functions applied to the MITC element in the context of RM plates. Concerning thin shell theory, Belytschko and Areias [33] proposed an XFEM formulation for thin-shell structures, Bayesteh and Mohammadi [34] studied the effect of crack tip enrichment functions in the analysis of shells, while Nguyen-Thanh et al. studied [35] a X–IGA shell formulation based on the Kirchhoff–Love theory. To the best of the authors knowledge, in pure Kirchhoff–Love plate theory the only works available are the ones of Lasry et al. [36,37], where an XFEM formulation is proposed.

1.5. Structure of the paper

In this paper, we develop an extended spline-based formulation for a cracked Kirchhoff–Love plate, using a GIFT framework, employing NURBS for the geometry parameterization and PHT-Splines for the field variable, and enrich solution with the Heaviside function and crack tip asymptotic expansions. Mainly, we address the efficiency of adaptive refinement over uniform refinement by using a recovery-based error estimator to drive the local adaptivity.

The remainder of the paper is organized as follows. A brief introduction to the plate theory, with its strong and weak forms, is given in Section 2, the modal analysis of plates is summarized in Section 3. Section 4 is devoted to the extended formulation of GIFT, while in Section 5 the computation of the stress intensity factors is outlined. In Section 6, the error estimator and adaptive refinement algorithm are explained. Section 7 deals with numerical examples and finally the main results are summarized in Section 8.

The numerical implementation was done in Matlab®, based on the open-source package IGAPACK, available at https://github.com/canitesc/IGAPack. In particular, the X–IGA routines were inspired by the open-source code IGAFEM [38], available at https://sourceforge.net/projects/cmcodes/. The numerical examples presented in this paper were carried out using the HPC facilities of the University of Luxembourg – see https://hpc.uni.lu.

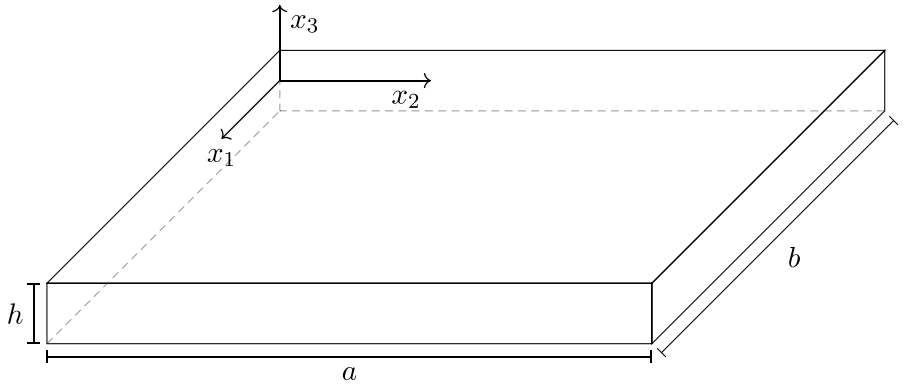

Fig. 1. Plate geometry and reference system.

2. Kirchhoff–Love plate theory

Let $\Omega \subset \mathbb{R}^2$ be an open-bounded region with boundary Γ. We consider a plate occupying a domain $V = \Omega \times \left[\frac{-h}{2}, \frac{h}{2}\right]$, where h is the thickness. It is assumed that the material plate is homogeneous and isotropic, with Young's modulus E and Poisson's ratio ν (see Fig. 1).

The displacement $\mathbf{u} = \{u_1, u_2, u_3\}^T$ under the Kirchhoff–Love theory can be written as

$$\begin{aligned} u_1(x_1, x_2, x_3) &= -x_3 \partial_1 u(x_1, x_2) \\ u_2(x_1, x_2, x_3) &= -x_3 \partial_2 u(x_1, x_2) \\ u_3(x_1, x_2, x_3) &= u(x_1, x_2) \end{aligned} \tag{1}$$

where the notation $\partial_\alpha(\cdot)$ represents the partial derivative with respect to x_α. In the Kirchhoff–Love model, the kinematic actions are such that the normal vectors to the undeformed reference surface remain orthogonal to the deformed surface and does not change in length. Thus, the transverse shear strains are zero.

The strains in terms of the displacements are given by:

$$\boldsymbol{\varepsilon} = \begin{Bmatrix} \varepsilon_{11} \\ \varepsilon_{22} \\ \varepsilon_{12} \end{Bmatrix} = \begin{Bmatrix} -x_3 \partial_{11} u \\ -x_3 \partial_{22} u \\ -2x_3 \partial_{12} u \end{Bmatrix} \tag{2}$$

while the stresses are given by

$$\boldsymbol{\sigma} = \begin{Bmatrix} \sigma_{11} \\ \sigma_{22} \\ \sigma_{12} \end{Bmatrix} = \frac{E}{(1-\nu^2)} \begin{bmatrix} 1 & \nu & 0 \\ \nu & 1 & 0 \\ 0 & 0 & \dfrac{(1-\nu)}{2} \end{bmatrix} \begin{Bmatrix} \varepsilon_{11} \\ \varepsilon_{22} \\ \varepsilon_{12} \end{Bmatrix} \tag{3}$$

which can be written as

$$\boldsymbol{\sigma} = \frac{E}{(1-\nu^2)} \mathbf{D} \boldsymbol{\varepsilon} \tag{4}$$

where $\mathbf{D}$ is the constitutive matrix:

$$\mathbf{D} = D \begin{bmatrix} 1 & \nu & 0 \\ \nu & 1 & 0 \\ 0 & 0 & (1-\nu)/2 \end{bmatrix} \tag{5}$$

and D is known as the plate bending stiffness

$$D = \frac{Eh^3}{12(1-\nu^2)} \tag{6}$$

The bending moments are defined as

$$\mathbf{m} = \begin{Bmatrix} m_{11} \\ m_{22} \\ m_{12} \end{Bmatrix} = D \begin{bmatrix} 1 & \nu & 0 \\ \nu & 1 & 0 \\ 0 & 0 & \dfrac{(1-\nu)}{2} \end{bmatrix} \begin{Bmatrix} -\partial_{11} u \\ -\partial_{22} u \\ -2\partial_{12} u \end{Bmatrix} \tag{7}$$

Finally, the shear forces are defined as

$$\mathbf{Q} = \begin{Bmatrix} Q_1 \\ Q_2 \end{Bmatrix} = \begin{Bmatrix} -D\left(\partial_{111} u + \partial_{122} u\right) \\ -D\left(\partial_{222} u + \partial_{112} u\right) \end{Bmatrix} \tag{8}$$

2.1. Strong form

The outward unit normal vector to the boundary is $\mathbf{n}$, and $\mathbf{s}$ is the unit tangent vector such that $\mathbf{n} \times \mathbf{s} = x_3$. Greek indices, α and β, take the values 1 and 2 respectively, and repeated indices imply summation. Normal and tangential components are denoted $(\cdot)_n = ()_\alpha n_\alpha$ and $(\cdot)_s = ()_\alpha s_\alpha$, respectively.

If the boundary Γ is not smooth, the corners, where the normal undergoes a discontinuity, are denoted $\partial\Gamma = x_c$. Here, $x_c \in \Gamma$, $c = 1, 2, \ldots$ are the corner locations.

Applying all the constitutive equations presented on the previous section, we obtain the following boundary-value problem (BVP) for the Kirchhoff–Love plate theory [39]:

$$\begin{array}{rcc} -D\partial_{\alpha\beta} m_{\alpha\beta} = q & \text{in} & \Omega \\ u = W & \text{on} & \Gamma_W \\ \partial_n u = \Theta & \text{on} & \Gamma_\Theta \\ m_{nn} = M_n & \text{on} & \Gamma_M \\ \partial_\alpha m_{n\alpha} + \partial_s m_{ns} = Q + \partial s M_s & \text{on} & \Gamma_Q \\ [m_{ns}] = [M_s] & \text{on} & \partial\Gamma \cap \Gamma_Q \end{array} \tag{9}$$

where q is the distributed loading on the plate, W is the prescribed displacement on Γ_W of the plate, Θ is the prescribed rotation on Γ_Θ, M_n the prescribed normal bending moment on Γ_M, M_s and Q the prescribed tangential bending moment and shear force on Γ_Q, respectively, and $[M_s]$ represents a corner force imposed on non smooth domains. Γ_W, Γ_Θ, Γ_M and Γ_Q are subsets of the boundary Γ, where the different types of boundary conditions are applied.

2.2. Weak form using GIFT

The variational formulation or weak form of the Kirchhoff–Love plate theory corresponds to finding a function $u \in H^2(\Omega)$ that satisfies $u = W$ on Γ_W and $\partial_n u = \Theta$ on Γ_Θ such that for any $v \in H^2(\Omega)$ with $v = 0$ on Γ_W and $\partial_n v = 0$ on Γ_Θ:

$$a(v, u) = l(v) \tag{10}$$

$$a(v, u) = D \int_\Omega \left[\nu \Delta u \delta_{\alpha\beta} + (1-\nu)\partial_{\alpha\beta} u\right] \partial_{\alpha\beta} v \mathrm{d}\Omega \tag{11}$$

$$l(v) = \int_\Omega q v \mathrm{d}\Omega + \int_{\Gamma_Q} \left(Q + \partial_s M_s\right) v \mathrm{d}\Gamma - \int_{\Gamma_M} M_n \partial_n v \mathrm{d}\Gamma - [M_s] v \tag{12}$$

The plate domain Ω is parameterized on a parametric domain Ξ by a mapping function $\mathbf{F}$:

$$\boldsymbol{x} := \mathbf{F}(\boldsymbol{\xi}) = \sum_{i \in I} \mathbf{C}_i N_i(\boldsymbol{\xi}) \tag{13}$$

where $\boldsymbol{x}$ are the coordinates in the physical space, $\mathbf{C}_i$ are the control points, $N_i(\boldsymbol{\xi})$ are the NURBS basis functions and I denotes the set of indices employed for the geometry.

The unknown field u_h of the boundary value problem can be approximated with a different finite dimensional space, whereas for this work we choose the PHT-splines basis $M_i(\boldsymbol{\xi})$. The approximation can be defined with the

help of the inverse of the mapping $\mathbf{F}$ as:

$$u_h(\boldsymbol{x}) = \sum_{k\in J} U_k (M_k \circ \mathbf{F}^{-1})(\boldsymbol{x}) \tag{14}$$

where U_k are the control variables corresponding to basis functions $M_k(\boldsymbol{\xi})$ and J denotes the set of indices employed for the PHT-splines basis functions.

Using the approximations for u_h, taking $v = \{M_k\}_{k\in J}$, and replacing it in Eq. (10), the discretized version of the weak form can be written as the following linear system of equation:

$$\mathbf{KU} = \mathbf{f} \tag{15}$$

where $\mathbf{K}$ is known as the stiffness matrix, $\mathbf{U}$ as the vertical control displacement solution of the plate and $\mathbf{f}$ as the force vector. The coefficients of the stiffness matrix $\mathbf{K}$ and the force vector $\mathbf{f}$ are given, respectively, by:

$$\mathbf{K}_{ij} = D\int_\Omega \left[\nu\Delta\left(M_i \circ \mathbf{F}^{-1}\right)\delta_{\alpha\beta} + (1-\nu)\partial_{\alpha\beta}\left(M_i \circ \mathbf{F}^{-1}\right)\right]\partial_{\alpha\beta}\left(M_j \circ \mathbf{F}^{-1}\right)\mathrm{d}\Omega \tag{16}$$

$$\begin{aligned}\mathbf{f}_j = &\int_\Omega q\left(M_j \circ \mathbf{F}^{-1}\right)\mathrm{d}\Omega + \int_{\Gamma_Q}\left(Q + \partial_s M_s\right)\left(M_j \circ \mathbf{F}^{-1}\right)\mathrm{d}\Gamma \\ &- \int_{\Gamma_M} M_n\partial_n\left(M_j \circ \mathbf{F}^{-1}\right)\mathrm{d}\Gamma - [M_s]\left(M_j \circ \mathbf{F}^{-1}\right)\end{aligned} \tag{17}$$

Also, the stiffness matrix and the force vector can be denoted by the following matrix products [40]:

$$\mathbf{K} = \int_\Omega \mathbf{B}\mathbf{D}\mathbf{B}^{\mathbf{T}}\mathrm{d}\Omega \tag{18}$$

with

$$\mathbf{B} = \begin{bmatrix} -\partial_{11}\left(M_1 \circ \mathbf{F}^{-1}\right) & -\partial_{11}\left(M_2 \circ \mathbf{F}^{-1}\right) & \cdots & -\partial_{11}\left(M_{n-1} \circ \mathbf{F}^{-1}\right) & -\partial_{11}\left(M_n \circ \mathbf{F}^{-1}\right) \\ -\partial_{22}\left(M_1 \circ \mathbf{F}^{-1}\right) & -\partial_{22}\left(M_2 \circ \mathbf{F}^{-1}\right) & \cdots & -\partial_{22}\left(M_{n-1} \circ \mathbf{F}^{-1}\right) & -\partial_{22}\left(M_n \circ \mathbf{F}^{-1}\right) \\ -2\partial_{12}\left(M_1 \circ \mathbf{F}^{-1}\right) & -2\partial_{12}\left(M_2 \circ \mathbf{F}^{-1}\right) & \cdots & -2\partial_{12}\left(M_{n-1} \circ \mathbf{F}^{-1}\right) & -2\partial_{12}\left(M_n \circ \mathbf{F}^{-1}\right) \end{bmatrix}^T \tag{19}$$

The force vector is written as

$$\mathbf{f} = \int_\Omega q\mathbf{N}\mathrm{d}\Omega + \int_{\Gamma_Q}\left(Q + \partial_s M_s\right)\mathbf{N}\mathrm{d}\Gamma - \int_{\Gamma_M} M_n\partial_n\mathbf{N}\mathrm{d}\Gamma - [M_s]\mathbf{N} \tag{20}$$

with

$$\mathbf{N} = \begin{bmatrix}\left(M_1 \circ \mathbf{F}^{-1}\right) & \left(M_2 \circ \mathbf{F}^{-1}\right) & \cdots & \left(M_{n-1} \circ \mathbf{F}^{-1}\right) & \left(M_n \circ \mathbf{F}^{-1}\right)\end{bmatrix}^T \tag{21}$$

$$\mathbf{dN} = \begin{bmatrix} \partial_1\left(M_1 \circ \mathbf{F}^{-1}\right) & \partial_1\left(M_2 \circ \mathbf{F}^{-1}\right) & \cdots & \partial_1\left(M_{n-1} \circ \mathbf{F}^{-1}\right) & \partial_1\left(M_n \circ \mathbf{F}^{-1}\right) \\ \partial_2\left(M_1 \circ \mathbf{F}^{-1}\right) & \partial_2\left(M_2 \circ \mathbf{F}^{-1}\right) & \cdots & \partial_2\left(M_{n-1} \circ \mathbf{F}^{-1}\right) & \partial_2\left(M_n \circ \mathbf{F}^{-1}\right) \end{bmatrix}^{\mathbf{T}} \tag{22}$$

$$\partial_n\mathbf{N} = \mathbf{dN}\cdot\mathbf{n} \tag{23}$$

In the previous equations $\partial_i\left(M_k \circ \mathbf{F}^{-1}\right)$ and $\partial_{ik}\left(M_k \circ \mathbf{F}^{-1}\right)$ are the first and second derivatives with respect to the geometry $\boldsymbol{x}(\boldsymbol{\xi}) = (x_1, x_2)$ computed by the chain rule, while n is the number of PHT-splines basis functions.

3. Vibration of plates

The strong form of the dynamic equilibrium equation for homogeneous and isotropic plates can be expressed by including the mass density ρ and plate thickness h into Eq. (9)

$$-D\partial_{\alpha\beta}m_{\alpha\beta} + \rho h\ddot{u} = q \tag{24}$$

Considering that there is no damping or external loads acting on the plate, the equation of motion can be expressed in the following weak form:

$$D\int_\Omega \left[\nu\Delta u\delta_{\alpha\beta} + (1-\nu)\partial_{\alpha\beta}u\right]\partial_{\alpha\beta}v\mathrm{d}\Omega + \int_\Omega v\rho h\ddot{u}d\Omega = 0 \tag{25}$$

Analogously to the previous section, the discretized weak form can be written as

$$\mathbf{M}\ddot{\mathbf{U}} + \mathbf{K}\mathbf{U} = 0 \tag{26}$$

where $\mathbf{K}$ is the aforementioned stiffness matrix and $\mathbf{M}$ is known as the mass matrix, given by:

$$\mathbf{M} = \int_{\Omega} \rho h \mathbf{N}\mathbf{N}^{\mathbf{T}} d\Omega \tag{27}$$

The general solution of Eq. (26) that describes the unforced and undamped vibrations of a solid is [40]:

$$u = \overline{u} e^{i\omega t} \tag{28}$$

In this equation, i is the imaginary unit, ω is the natural frequency, t is the time and $\overline{u}$ is the eigenvector associated with ω. By substituting this solution in the Eq. (28) [41], the natural frequencies of the plate can be found by solving the following eigenvalue problem:

$$\left(\mathbf{K} - \omega^2 \mathbf{M}\right) \overline{\mathbf{U}} = 0 \tag{29}$$

where $\overline{\mathbf{U}}$ is a matrix containing the eigenvectors associated to the eigenvalues w. The equation of eigenvalues has a non-trivial solution when it is fulfilled that:

$$\det\left(\mathbf{K} - \omega^2 \mathbf{M}\right) = 0 \tag{30}$$

This last equation yields a discrete set of eigenvalues ω_i, with $i = 1, 2, 3, \ldots$; where each ω_i has an associated vector $\overline{\mathbf{U}}_i$, as shown in the following equation [38]:

$$\left(\mathbf{K} - \omega_i^2 \mathbf{M}\right) \overline{\mathbf{U}}_i = 0 \tag{31}$$

4. X–GIFT: Extended formulation for GIFT

In presence of a crack, the field approximation (Eq. (14)) is enriched by additional degrees of freedom, representing the jump of displacement across the crack (Heaviside function) and a set of functions representing the asymptotic behavior of the solution near the crack tip, i.e.

$$u(\boldsymbol{x}) = \sum_{k \in J} \boldsymbol{U}_k M_k \circ \mathbf{F}^{-1}(\boldsymbol{x}) + \sum_{k \in L} M_k \circ \mathbf{F}^{-1}(\boldsymbol{x}) H(\boldsymbol{x}) \boldsymbol{d}_k + \sum_{k \in M} M_k \circ \mathbf{F}^{-1}(\boldsymbol{x}) \left(\sum_{i=1}^{4} F_i(r, \theta) \boldsymbol{c}_k^i \right) \tag{32}$$

where $\boldsymbol{U}_k$ are the regular unknown variables from Eq. (14), $\boldsymbol{d}_k$ and $\boldsymbol{c}_k^i$ are the additional DOF related to the crack face and crack tip enrichment, respectively. The set J is the set of indices for the PHT-Splines basis functions, while the sets L and M are the sets of indices for crack face and crack tip enriched DOF, respectively.

The Heaviside function is defined as follows:

$$H(\boldsymbol{x}) = \begin{cases} 1 \text{ for nodes on one side of the crack} \\ -1 \text{ for nodes on another side of the crack} \end{cases} \tag{33}$$

The basis functions for the crack tip enrichment are defined as:

$$\{F_k(r, \theta)\} = \left\{ r^{3/2} \sin\left(\frac{3\theta}{2}\right), r^{3/2} \cos\left(\frac{3\theta}{2}\right), r^{3/2} \sin\left(\frac{\theta}{2}\right), r^{3/2} \cos\left(\frac{\theta}{2}\right) \right\} \tag{34}$$

where (r, θ) is the local polar coordinate system at the crack tip (see Fig. 2).

The transformation between the local polar coordinate system to the local Cartesian coordinate system at the crack tip is given as follows:

$$\begin{cases} r = \sqrt{{x_1^l}^2 + {x_2^l}^2} \\ \theta = \arctan\left(\dfrac{x_2^l}{x_1^l}\right) \end{cases} \tag{35}$$

The following is the transformation between the local Cartesian coordinate system (x_1^l, x_2^l) at the crack tip and the physical coordinates:

$$\begin{Bmatrix} x_1^l \\ x_2^l \end{Bmatrix} = \begin{bmatrix} \cos(\phi) & \sin(\phi) \\ -\sin(\phi) & \cos(\phi) \end{bmatrix} \begin{Bmatrix} x_1 - x_1^{ct} \\ x_2 - x_2^{ct}, \end{Bmatrix} \tag{36}$$

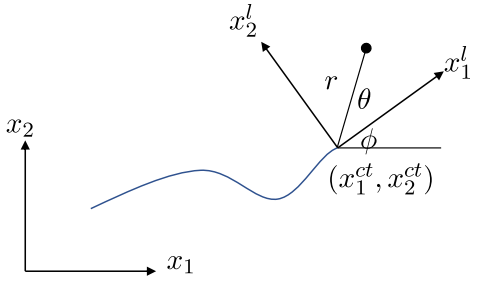

Fig. 2. Local and global coordinates at the crack tip. (x_1, x_2) are the global coordinates, while (x_1^{ct}, x_2^{ct}) are the coordinates of the crack tip in the global system. ϕ is the angle between the crack tip and the horizontal line. (x_1^l, x_2^l) are the local coordinates rotated with respect to ϕ, and (r, θ) are the polar coordinates defined at (x_1^l, x_2^l). The blue line represents the crack. (For interpretation of the references to color in this figure legend, the reader is referred to the web version of this article.)

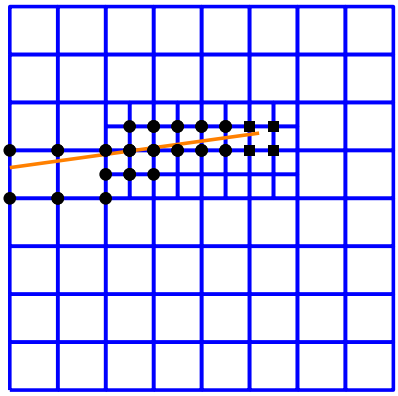

Fig. 3. Illustration of the enriched vertices on a T-mesh. The orange thick line denotes the crack. The black dots denote the Heaviside enriched vertices, while the black squares denote the crack tip enriched vertex. (For interpretation of the references to color in this figure legend, the reader is referred to the web version of this article.)

where (x_1, x_2) are the physical coordinates defined by Eq. (13), (x_1^{ct}, x_2^{ct}) are the crack tip coordinates at the physical space and ϕ is the angle between the crack tip with respect to the horizontal line.

Two types of crack tip enrichment criteria can be applied, namely the geometrical enrichment and the topological enrichment [42]. In the former, only the element containing the crack tip is enriched (i.e. the shape functions with the support in the crack tip element), while in the latter, the enrichment area remains constant in the refinement process. We implemented and compared both approaches. Our studies indicate that topological enrichment is significantly more efficient and accurate when it is coupled with adaptive refinement, and therefore it was used in all numerical examples in Section 7.

The level set method is a numerical method used to track interfaces and shapes. It was originally introduced by Osher and Sethian [43] for tracking the evolution of moving boundaries and now is typically used in XFEM method [44] or X–IGA method [26] to identify discontinuities in the domain, such as cracks, inclusions or voids.

In this work, we employ two level set functions to select which elements in the field discretization (Eq. (14)) should be enriched by the Heaviside or crack tip functions. Fig. 3 illustrates an example of (topologically) enriched vertices of a T-mesh.

Using the generalized formulation for the unknown vector given by Eq. (32), Eq. (15) and the level set method to identify elements enriched with the Heaviside and crack tip functions, the generalized linear system is given by:

$$\mathbf{K_{enr}U_{enr}} = \mathbf{f_{enr}}, \tag{37}$$

where the displacement control variables and additional enrichment DOFs are as follows:

$$\mathbf{U_{enr}} = \left\{\mathbf{U} \quad \mathbf{d} \quad \mathbf{c_1} \quad \mathbf{c_2} \quad \mathbf{c_3} \quad \mathbf{c_4}\right\}^{\mathbf{T}} \tag{38}$$

where $\mathbf{U}$, $\mathbf{d}$ and $\mathbf{c_i}$, $i = 1, 2, 3, 4$, are the vectors of regular DOF, crack face DOF and crack tip DOF, respectively. The stiffness matrix enriched $\mathbf{K_{enr}}$ is a generalization for Eq. (18) and is given by:

$$\mathbf{K_{enr}} = \int_{\Omega} \mathbf{B_{enr}} \mathbf{D} \mathbf{B_{enr}^T} \mathrm{d}\Omega \tag{39}$$

with $\mathbf{B_{enr}}$ defined as

$$\mathbf{B_{enr}} = \begin{bmatrix} \mathbf{B} & \mathbf{B_d} & \mathbf{B_{c_1}} & \mathbf{B_{c_2}} & \mathbf{B_{c_3}} & \mathbf{B_{c_4}} \end{bmatrix}^{\mathbf{T}} \tag{40}$$

$$\mathbf{B} = \begin{bmatrix} -\partial_{11} N_1^* & -\partial_{11} N_2^* & \cdots & -\partial_{11} N_{n-1}^* & -\partial_{11} N_n^* \\ -\partial_{22} N_1^* & -\partial_{22} N_2^* & \cdots & -\partial_{22} N_{n-1}^* & -\partial_{22} N_n^* \\ -2\partial_{12} N_1^* & -2\partial_{12} N_2^* & \cdots & -2\partial_{12} N_{n-1}^* & -2\partial_{12} N_n^* \end{bmatrix} \tag{41}$$

$$\mathbf{B_d} = \begin{bmatrix} -\partial_{11} N_1^* H & -\partial_{11} N_2^* H & \cdots & -\partial_{11} N_{n_{cf}-1}^* H & -\partial_{11} N_{n_{cf}}^* H \\ -\partial_{22} N_1^* H & -\partial_{22} N_2^* H & \cdots & -\partial_{22} N_{n_{cf}-1}^* H & -\partial_{22} N_{n_{cf}}^* H \\ -2\partial_{12} N_1^* H & -2\partial_{12} N_2^* H & \cdots & -2\partial_{12} N_{n_{cf}-1}^* H & -2\partial_{12} N_{n_{cf}}^* H \end{bmatrix} \tag{42}$$

$$\mathbf{B_{c_i}} = \begin{bmatrix} -\partial_{11}\left(N_1^* F_i\right) & -\partial_{11}\left(N_2^* F_i\right) & \cdots & -\partial_{11}\left(N_{n_{ct}-1}^* F_i\right) & -\partial_{11}\left(N_{n_{ct}}^* F_i\right) \\ -\partial_{22}\left(N_1^* F_i\right) & -\partial_{22}\left(N_2^* F_i\right) & \cdots & -\partial_{22}\left(N_{n_{ct}-1}^* F_i\right) & -\partial_{22}\left(N_{n_{ct}}^* F_i\right) \\ -2\partial_{12}\left(N_1^* F_i\right) & -2\partial_{12}\left(N_2^* F_i\right) & \cdots & -2\partial_{12}\left(N_{n_{ct}-1}^* F_i\right) & -2\partial_{12}\left(N_{n_{ct}}^* F_i\right) \end{bmatrix}, \quad i = 1, 2, 3, 4 \tag{43}$$

where n is the number of PHT-Splines basis functions, n_{cf} the number of Heaviside enriched basis functions, and n_{ct} the number of crack tip enriched basis functions. Analogously, the enriched force $\mathbf{f_{enr}}$ and mass $\mathbf{M_{enr}}$ are the generalizations of Eqs. (20) and (27), respectively:

$$\mathbf{f_{enr}} = \int_{\Omega} q \mathbf{N_{enr}} \mathrm{d}\Omega + \int_{\Gamma_Q} \left(Q + \partial_s M_s\right) \mathbf{N_{enr}} \mathrm{d}\Gamma - \int_{\Gamma_M} M_n \partial_n \mathbf{N_{enr}} \mathrm{d}\Gamma - [M_s] \mathbf{N_{enr}} \tag{44}$$

$$\mathbf{M_{enr}} = \int_{\Omega} \rho h \mathbf{N_{enr}} \mathbf{N_{enr}^T} d\Omega \tag{45}$$

where

$$\mathbf{N_{enr}} = \begin{bmatrix} \mathbf{N} & \mathbf{N_d} & \mathbf{N_{c_1}} & \mathbf{N_{c_2}} & \mathbf{N_{c_3}} & \mathbf{N_{c_4}} \end{bmatrix}^{\mathbf{T}} \tag{46}$$

$$\mathbf{N} = \begin{bmatrix} N_1^* & N_2^* & \cdots & N_{n-1}^* & N_n^* \end{bmatrix} \tag{47}$$

$$\mathbf{N_d} = \begin{bmatrix} N_1^* H & N_2^* H & \cdots & N_{n_{cf}-1}^* H & N_{n_{cf}}^* H \end{bmatrix} \tag{48}$$

$$\mathbf{N_{c_i}} = \begin{bmatrix} N_1^* F_i & N_2^* F_i & \cdots & N_{n_{ct}-1}^* F_i & N_{n_{ct}}^* F_i \end{bmatrix}, \quad i = 1, 2, 3, 4 \tag{49}$$

$$\mathbf{dN_{enr}} = \begin{bmatrix} \mathbf{dN} & \mathbf{dN_d} & \mathbf{dN_{c_1}} & \mathbf{dN_{c_2}} & \mathbf{dN_{c_3}} & \mathbf{dN_{c_4}} \end{bmatrix}^{\mathbf{T}} \tag{50}$$

$$\mathbf{dN} = \begin{bmatrix} \partial_1 N_1^* & \partial_1 N_2^* & \cdots & \partial_1 N_{n-1}^* & \partial_1 N_n^* \\ \partial_2 N_1^* & \partial_2 N_2^* & \cdots & \partial_2 N_{n-1}^* & \partial_2 N_n^* \end{bmatrix} \tag{51}$$

$$\mathbf{dN_d} = \begin{bmatrix} \partial_1 N_1^* H & \partial_1 N_2^* H & \cdots & \partial_1 N_{n_{cf}-1}^* H & \partial_1 N_{n_{cf}}^* H \\ \partial_2 N_1^* H & \partial_2 N_2^* H & \cdots & \partial_2 N_{n_{cf}-1}^* H & \partial_2 N_{n_{cf}}^* H \end{bmatrix} \tag{52}$$

$$\mathbf{dN_{c_i}} = \begin{bmatrix} \partial_1\left(N_1^* F_i\right) & \partial_1\left(N_2^* F_i\right) & \cdots & \partial_1\left(N_{n_{ct}-1}^* F_i\right) & \partial_1\left(N_{n_{ct}}^* F_i\right) \\ \partial_2\left(N_1^* F_i\right) & \partial_2\left(N_2^* F_i\right) & \cdots & \partial_2\left(N_{n_{ct}-1}^* F_i\right) & \partial_2\left(N_{n_{ct}}^* F_i\right) \end{bmatrix}, \quad i = 1, 2, 3, 4 \tag{53}$$

$$\mathbf{dN_n^{enr}} = \mathbf{dN_{enr}} \cdot \mathbf{n} \tag{54}$$

Again, in the previous equations $\partial_i N_k^*$ and $\partial_{ik} N_k^*$ are the first and second derivatives with respect to the geometry $\boldsymbol{x}(\boldsymbol{\xi}) = (x_1, x_2)$ computed by the chain rule. And N_k^* denotes the composition between the physical mapping and the field basis $M_k \circ \mathbf{F}^{-1}$.

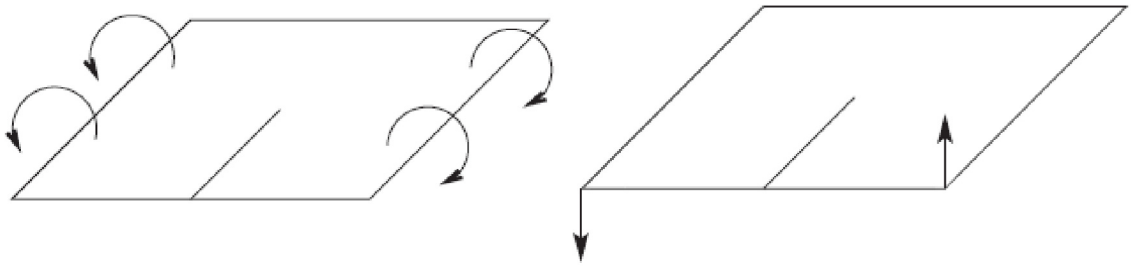

(a) k_1 (b) k_2

Fig. 4. Loading modes for Kirchhoff–Love plate theory: (a) Symmetric bending (k_1) and (b) Anti-symmetric bending (k_2).

5. Computation of stress intensity factors (SIF)

In this section, we briefly explain the theory and procedure employed to compute the stress intensity factors in the context of the Kirchhoff–Love plate theory.

5.1. Asymptotic displacement near the crack tip and fracture modes

In the Kirchhoff–Love plate theory, there are two fracture modes depending on the loading type: a symmetric bending, known as mode k_1, and anti-symmetric bending mode k_2. Both fracture modes are shown in Fig. 4.

The stress field close to the tip of a through crack in a plate was first obtained by Williams [45] in the context of Kirchhoff–Love plate model using an eigenfunction approach to solve the bi-harmonic equation, given by Eq. (9). The asymptotic displacement field u_{asymp} is given by [46]:

$$u_{asymp} = \frac{(2r)^{\frac{3}{2}}(1-\nu^2)}{2Eh(3+\nu)}\left\{k_1\left[\frac{1}{3}\left(\frac{7+\nu}{1-\nu}\right)\cos\left(\frac{3\theta}{2}\right)-\cos\left(\frac{\theta}{2}\right)\right] + k_2\left[\frac{1}{3}\left(\frac{5+3\nu}{1-\nu}\right)\sin\left(\frac{3\theta}{2}\right)-\sin\left(\frac{\theta}{2}\right)\right]\right\}, \tag{55}$$

where k_1 and k_2 are defined as:

$$k_1 = \lim_{r\to 0}\sqrt{2r}\sigma_{\theta\theta}\,(r,0) \quad , \quad k_2 = \lim_{r\to 0}\left(\frac{3+\nu}{1+\nu}\right)\sqrt{2r}\sigma_{r\theta}\,(r,0) \tag{56}$$

The stress field due to bending for the Kirchhoff–Love plate theory, in polar coordinates (r,θ) with respect to the crack tip, are given as follows [35,47]:

$$\begin{Bmatrix}\sigma_{rr}\\ \sigma_{\theta\theta}\\ \sigma_{r\theta}\end{Bmatrix} = k_1\frac{x_3}{2h\sqrt{2r}(3+\nu)}\begin{Bmatrix}(3+5\nu)\cos\left(\frac{\theta}{2}\right)-(7+\nu)\cos\left(\frac{3\theta}{2}\right)\\ (5+3\nu)\cos\left(\frac{\theta}{2}\right)+(7+\nu)\cos\left(\frac{3\theta}{2}\right)\\ -(1-\nu)\sin\left(\frac{\theta}{2}\right)+(7+\nu)\sin\left(\frac{3\theta}{2}\right)\end{Bmatrix} + k_2\frac{x_3}{2h\sqrt{2r}(3+\nu)}\begin{Bmatrix}-(3+5\nu)\sin\left(\frac{\theta}{2}\right)+(5+3\nu)\sin\left(\frac{3\theta}{2}\right)\\ -(5+3\nu)\left(\sin\left(\frac{\theta}{2}\right)+\sin\left(\frac{3\theta}{2}\right)\right)\\ (\nu-1)\cos\left(\frac{\theta}{2}\right)+(5+3\nu)\cos\left(\frac{3\theta}{2}\right)\end{Bmatrix} \tag{57}$$

The relation between the stress in polar coordinates with the local coordinates with respect to the crack tip is given by

$$\begin{Bmatrix} \sigma_{rr} \\ \sigma_{\theta\theta} \\ \sigma_{r\theta} \end{Bmatrix} = \begin{bmatrix} \cos^2(\phi) & \sin^2(\phi) & 2\sin(\phi)\cos(\phi) \\ \sin^2(\phi) & \cos^2(\phi) & -2\sin(\phi)\cos(\phi) \\ -\sin(\phi)\cos(\phi) & \sin(\phi)\cos(\phi) & \cos^2(\phi)-\sin^2(\phi) \end{bmatrix} \begin{Bmatrix} \sigma_{11}^{l} \\ \sigma_{22}^{l} \\ \sigma_{12}^{l} \end{Bmatrix} \tag{58}$$

where ϕ is the angle defined in Section 4. The previous stress relationship can also be written in the following matrix form as

$$\boldsymbol{\sigma}_{polar} = \mathbf{T}(\phi)\boldsymbol{\sigma}_{local} \tag{59}$$

The inverse relationship also holds:

$$\boldsymbol{\sigma}_{local} = \mathbf{T}^{-1}(\phi)\boldsymbol{\sigma}_{polar} \tag{60}$$

5.2. J-integral and interaction integral

J-integral is commonly used in fracture mechanics to determine SIF. In this work, we use the domain integral definition for a through-the-thickness crack with the crack front normal to the mid-surface [47,48], i.e.

$$J = \frac{1}{h}\int_{V^\star}\left(\sigma_{ij}\frac{\partial u_i}{\partial x_1} - \frac{1}{2}\sigma_{ij}\varepsilon_{ij}\delta_{1j}\right)\frac{\partial q}{\partial x_j}\mathrm{d}V \tag{61}$$

where $V^\star$ is an arbitrary volume that encloses the crack tip. Typically $V^\star$ is a hollow cylinder with the center line passing through the crack tip, perpendicular to the mid-plane (see [47] for more details). Function q is the weight function varying from 0 (the outer contour of $V^\star$) to 1 (the inner contour of $V^\star$). The relationship between the J-integral value and the stress intensity factors in the cases of mixed-mode loadings for the Kirchhoff–Love plate theory is given by [46]:

$$J = G = \frac{\pi}{3E}\left(\frac{1+\nu}{3+\nu}\right)\left(k_1^2 + k_2^2\right), \tag{62}$$

where k_1 and k_2 are the symmetric and anti-symmetric bending SIF [46]. To calculate the SIF for a particular mode of loading in cases of mixed-mode loading, we follow the scheme which was derived in [23,49] for two and three-dimensional problems. We consider two states of a cracked solid: corresponding to the present state $\left(\sigma_{ij}^{(1)}, \varepsilon_{ij}^{(1)}, u_i^{(1)}\right)$ and an auxiliary state $\left(\sigma_{ij}^{(2)}, \varepsilon_{ij}^{(2)}, u_i^{(2)}\right)$ which will be chosen as the numerical field and the asymptotic field, respectively. From Eq. (61), the domain form of the J-integral for the superposition of the two state is:

$$J^{(1+2)} = \frac{1}{h}\int_V\left[\left(\sigma_{ij}^{(1)}+\sigma_{ij}^{(2)}\right)\left(\frac{\partial u_i^{(1)}}{\partial x_1}+\frac{\partial u_i^{(2)}}{\partial x_1}\right) - \frac{1}{2}\left(\sigma_{ij}^{(1)}+\sigma_{ij}^{(2)}\right)\left(\varepsilon_{ij}^{(1)}+\varepsilon_{ij}^{(2)}\right)\delta_{1j}\right]\frac{\partial q}{\partial x_j}\mathrm{d}V \tag{63}$$

Expanding and grouping terms of similar states in Eq. (63), we can written this as:

$$J^{(1+2)} = J^{(1)} + J^{(2)} + I^{(1,2)} \tag{64}$$

where

$$J^{(\alpha)} = \frac{1}{h}\int_V\left(\sigma_{ij}^{(\alpha)}\frac{\partial u_i^{(\alpha)}}{\partial x_1} - \frac{1}{2}\sigma_{ij}^{(\alpha)}\varepsilon_{ij}^{(\alpha)}\delta_{1j}\right)\frac{\partial q}{\partial x_j}\mathrm{d}V \quad , \quad \alpha = 1,2 \tag{65}$$

And the definition of the interaction integral $I^{(1,2)}$ is given by:

$$I^{(1,2)} = \frac{1}{h}\int_V\left(\sigma_{ij}^{(1)}\frac{\partial u_i^{(2)}}{\partial x_1} + \sigma_{ij}^{(2)}\frac{\partial u_i^{(1)}}{\partial x_1} - \sigma_{ij}^{(1)}\varepsilon_{ij}^{(2)}\delta_{1j}\right)\frac{\partial q}{\partial x_j}\mathrm{d}V \tag{66}$$

Using Eq. (62), we obtain the J-integral for the combination of the states 1 and 2:

$$J^{(1+2)} = J^{(1)} + J^{(2)} + \frac{2\pi}{3E}\left(\frac{1+\nu}{3+\nu}\right)\left(k_1^{(1)}k_1^{(2)} + k_2^{(1)}k_2^{(2)}\right) \tag{67}$$

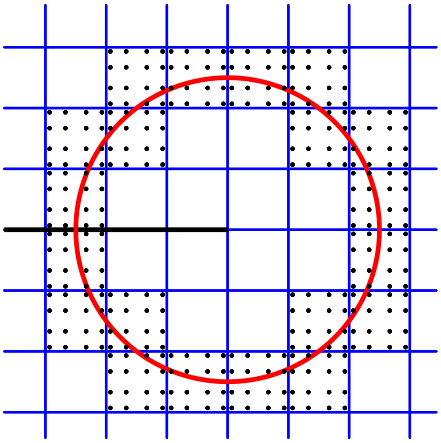

Fig. 5. J-integral: selected domain for the integration. Red line represents the circle of radius r_d, the black line represents the crack. (For interpretation of the references to color in this figure legend, the reader is referred to the web version of this article.)

Using Eqs. (64) and (67), the relationship between the interaction integral $I^{(1,2)}$, given by Eq. (66), and the stress intensity factors is:

$$I^{(1,2)} = \frac{2\pi}{3E}\left(\frac{1+\nu}{3+\nu}\right)\left(k_1^{(1)}k_1^{(2)} + k_2^{(1)}k_2^{(2)}\right) \tag{68}$$

To obtain the stress intensity factor, we choose the auxiliary state as one of the two modes of the plate: pure symmetric bending loading or pure anti-symmetric bending loading, as shown in Fig. 4; and then, we use the Eq. (68) to express $k_1^{(1)}$ and $k_2^{(1)}$:

$$\begin{aligned} k_1^{(1)} &= \frac{3E}{2\pi}\left(\frac{3+\nu}{1+\nu}\right) I^{(1,2)} \text{ with } k_1^{(2)} = 1, \quad k_2^{(2)} = 0 \\ k_2^{(1)} &= \frac{3E}{2\pi}\left(\frac{3+\nu}{1+\nu}\right) I^{(1,2)} \text{ with } k_1^{(2)} = 0, \quad k_2^{(2)} = 1 \end{aligned} \tag{69}$$

Accuracy of the J-integral evaluations depends significantly on the size of domain $V^\star$ enclosing the crack tip. In this work we use the domain, shown in Fig. 5 and defined by the elements that cut a circular cylinder with radius r_d centered at the crack tip axis. This approach was proposed in [47,50] where it was suggested to use r_d equal to 2.5 times the mean value of the square root of the fully cracked elements' areas. This strategy is further refereed as $r_d = 2.5\overline{a}$ in our results. In the present work we also compared this approach with other choices of r_d.

Finally, the weight function q is defined inside each PHT-spline element of the interaction integral domain as:

$$q = \sum_{i=1}^{4} N_i(x_1, x_2) q_i \tag{70}$$

where N_i are linear basis function, and the coefficients q_i are set to 1 for the vertices of the elements that lie on the inner boundary, and equal to zero if the node is on the outer boundary of $V^\star$.

6. Recovery-based error estimator and adaptive mesh refinement

Anitescu et al. [12] proposed a recovery-based error estimator for PHT-splines based on 2D and 3D linear elasticity. This definition was extended by Videla et al. [18] in the context of the Helmholtz equation. In the following section, the procedure to obtain the recovery-based error estimator is adapted to Kirchhoff–Love plate theory.

The main idea behind recovery-based error estimators is to create a more accurate approximation of the gradient of the solution utilizing for example, the super-convergent patch recovery procedure. Then, the recovered gradient solution is considered as a substitute for the exact gradient of the solution, which can be employed to compute error norms with high precision.

Table 1
Super-convergent points for splines of degree p and continuity C^{α} on interval $[-1, 1]$.

p	α	Super-convergent points
3	1	± 1, 0
4	1	$\pm\sqrt{(3/7) \pm (2/7)\sqrt{6/5}}$
5	2	± 1, $\pm\sqrt{1/3}$, 0
6	2	± 0.790208564, ± 0.2800702925
7	3	± 1, ± 0.5294113738, 0

The original procedure, proposed by Zienkiewicz and Zhu [51], consists in computing a more accurate solution at the carefully chosen points that are capable of generating a better approximation of the desired quantity. At those points, a higher-order polynomial fit is performed in order to obtain the recovered solution. Then, the error estimator is computed in the normalized H^2 semi-norm as [52]:

$$\frac{\|e_{rec}\|_{H^2}}{\|G\left[\mathbf{m}(u_h)\right]\|_{H^2}} = \frac{\left(\int_{\Omega} \left(G\left[\mathbf{m}(u_h)\right] - \mathbf{m}(u_h)\right)^T \mathbf{D}^{-1} \left(G\left[\mathbf{m}(u_h)\right] - \mathbf{m}(u_h)\right) d\Omega\right)^{1/2}}{\left(\int_{\Omega} \left(G\left[\mathbf{m}(u_h)\right]\right)^T \mathbf{D}^{-1} \left(G\left[\mathbf{m}(u_h)\right]\right) d\Omega\right)^{1/2}} \tag{71}$$

where $\mathbf{m}(u_h)$ is the numerical moment, computed using Eq. (7), $G\left[\mathbf{m}(u_h)\right]$ is the recovery moment computed using $\mathbf{m}(u_h)$. In the same way, the error indicator on each cell k can be computed as:

$$e_k = \left(\int_{\Omega} \left(G\left[\mathbf{m}(u_h)\right] - \mathbf{m}(u_h)\right)^T \mathbf{D}^{-1} \left(G\left[\mathbf{m}(u_h)\right] - \mathbf{m}(u_h)\right) d\Omega\right)^{1/2} \tag{72}$$

The carefully chosen points are the super-convergent points, which are computed in the same way as in [12]. Table 1 shows the super-convergent points on an interval $[-1, 1]$ for several values of spline degree p and continuity orders α.

Next, we briefly outline the procedure of computation of the recovery moment $G\left[\mathbf{m}(u_h)\right]$. The reader is referred to [12] for details regarding the implementation of this process with PHT-Splines.

Let be Ω be the domain and Ω_k, $k = 1, \ldots, n$ a set of n non-overlapping patches such that together they form Ω: $\cup_{k=1}^{n} \Omega_k = \Omega$. Let $\boldsymbol{x}^*_{i,k}$ $(i = 1, \ldots, N_k)$ be a set of N_k super-convergent points defined over the patch Ω_k. Let also $\phi^*_{i,k}$ be the set of basis functions employed for the recovery solution. In this case we employ B-splines functions of degree $p^* \geq p$ and continuity $\alpha^* \geq \alpha$. The $G\left[m(u_h)\right]$ is constructed as:

$$G\left[\mathbf{m}(u_h)\right](\boldsymbol{x}) = \sum \phi^*_{i,k}(\boldsymbol{x}) \boldsymbol{C}^*_{i,k} \tag{73}$$

where $\boldsymbol{C}^*_{i,k}$ are the new DOF associated with the recovery gradient solution. We require Eq. (73) to fulfill the condition:

$$G\left[\mathbf{m}(u_h)\right](\boldsymbol{x}^*_{i,k}) = \mathbf{m}(u_h)(\boldsymbol{x}^*_{i,k}) \tag{74}$$

Eq. (74) can be rewritten as the following linear system:

$$\boldsymbol{A}^k \boldsymbol{C}^*_k = \boldsymbol{b}^k \tag{75}$$

where

$$\boldsymbol{A}^k_{ij} = \phi^*_{j,k}(\boldsymbol{x}^*_{i,k}) \tag{76}$$

$$\boldsymbol{b}^k_i = D \begin{bmatrix} 1 & \nu & 0 \\ \nu & 1 & 0 \\ 0 & 0 & \dfrac{(1-\nu)}{2} \end{bmatrix} \begin{Bmatrix} -\partial_{11} u_h(\boldsymbol{x}^*_{i,k}) \\ -\partial_{22} u_h(\boldsymbol{x}^*_{i,k}) \\ -2\partial_{12} u_h(\boldsymbol{x}^*_{i,k}) \end{Bmatrix} \tag{77}$$

Finally, the recovery solution can be computed by solving Eq. (75).

After the recovery-based error estimator is calculated, the refinement is guided using "Dörfler marking" strategy [53]. The approach consists in sorting the elements according to their error contribution and then refining

elements until their total contribution to the error is bigger than a certain percentage α of the error estimator. In the following numerical experiments, unless other is specified, $\alpha = 75\%$ was used.

In the case of the dynamic analysis, two different schemes can drive adaptive refinement: the first one consists in taking each mode independently and perform adaptive refinement based on the recovery-based error estimator computed using that particular vibration mode. This scheme leads to high memory costs since for each vibration mode the corresponding refinement needs to be stored and processed. The second scheme consists in taking a particular static solution (for instance, the result for the clamped problem with constant loading) and using it to drive the adaptive refinement and compute the desired vibration modes.

In this work, both methods were tested and lead to similar results, therefore the second approach was employed due to its better computational efficiency.

Lastly, we say that the recovery-based error estimator is asymptotically exact if the ratio between the error estimator and the error itself tends to 1 as the mesh size h tends to 0, i.e.:

$$\theta(\Delta u_h, \Omega) := \frac{\|e_{rec}\|_{H^2}}{\|u - u_h\|_{H^2}} \rightarrow 1 ash \rightarrow 0 \tag{78}$$

where $\theta(\Delta u_h, \Omega)$ is known as the effectivity index of the error estimator.

7. Numerical examples

In this section, we present several numerical examples concerned with different static and dynamic behavior of Kirchhoff–Love plates with cracks.

For problems with known analytical solutions, we use the following relative H^2 semi-norm of the error:

$$\frac{\|u - u_h\|_{H^2}}{\|u\|_{H^2}} = \sqrt{\frac{\int_\Omega (\mathbf{m}(u) - \mathbf{m}(u_h))^T \mathbf{D}^{-1} (\mathbf{m}(u) - \mathbf{m}(u_h))\, d\Omega}{\int_\Omega (\mathbf{m}(u))^T \mathbf{D}^{-1} (\mathbf{m}(u))\, d\Omega}} \tag{79}$$

In all numerical examples in this section, crack faces are assumed traction and moment free.

7.1. Bending of plates with cracks

7.1.1. Square plate with an edge crack

In this first numerical example, we solve the problem of a plate with an edge crack of length a under non-homogeneous Dirichlet boundary conditions given by pure mode k_2:

$$u^{\text{exact}} = \frac{(2r)^{3/2}}{2Eh} \frac{(1-\nu^2)}{(3+\nu)} \left[\frac{3\nu + 5}{3(\nu - 1)} \sin\left(\frac{3\theta}{2}\right) - \sin\left(\frac{\theta}{2}\right) \right] \tag{80}$$

This problem is also solved in [36]. The non-homogeneous boundary conditions are imposed using Nitsche's approach [39,54], and both crack faces are moment and traction free.

The plate dimensions are: length $L = 1$, width $H = 1$, thickness $h = 0.09$ and crack length $a = 0.5$; while the material properties are: Young's modulus $E = 14.98$ [kPa], Poisson's ratio $\nu = 0.3$.

Fig. 6 shows the numerical vertical displacement obtained using PHT-splines of degree $p = q = 4$ with adaptive refinement. As it can be seen, the method is capable of modeling an anti-symmetric bending loading mode.

Fig. 7 shows the initial mesh and five different states of the adaptive refinement obtained using the recovery-based error estimator criteria. In these figures, we can see that the refinement process is centered around the tip of the crack. Similar patterns were observed in all simulations.

To impose the non-homogeneous Dirichlet boundary condition with Nitsche's method, we employed the stabilization parameters shown in Table 2 for three different PHT-splines degrees. Fig. 8 shows the relative L^2 error norm on the boundary for $p = 3, 4, 5$, and we can conclude that the Nitsche's method is capable of imposing the boundary conditions accurately and reliably.

Numerical results are first compared with the data, obtained by extended isogeometric analysis (X–IGA) with NURBS of degree $p = 4$ and continuity C^1, C^2 and C^3. For X–GIFT, NURBS of $p = 1$ and PHT-splines of $p = 4$ are employed. In all cases, solution is refined uniformly. Fig. 9 shows comparison of results in terms of the relative L^2 error norm vs. the degrees of freedom (Fig. 9a) and vs. the computational time (Fig. 9b). From Fig. 9a

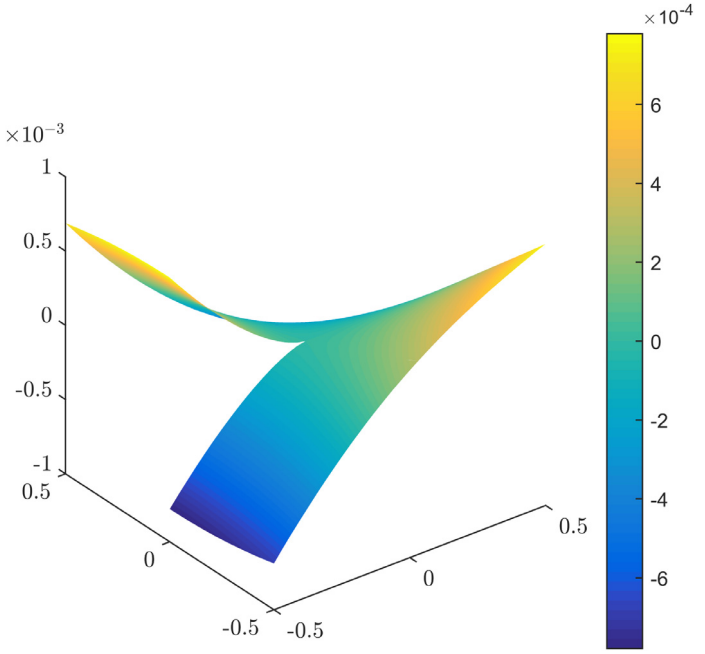

Fig. 6. Deformation of the infinite plate with a straight crack.

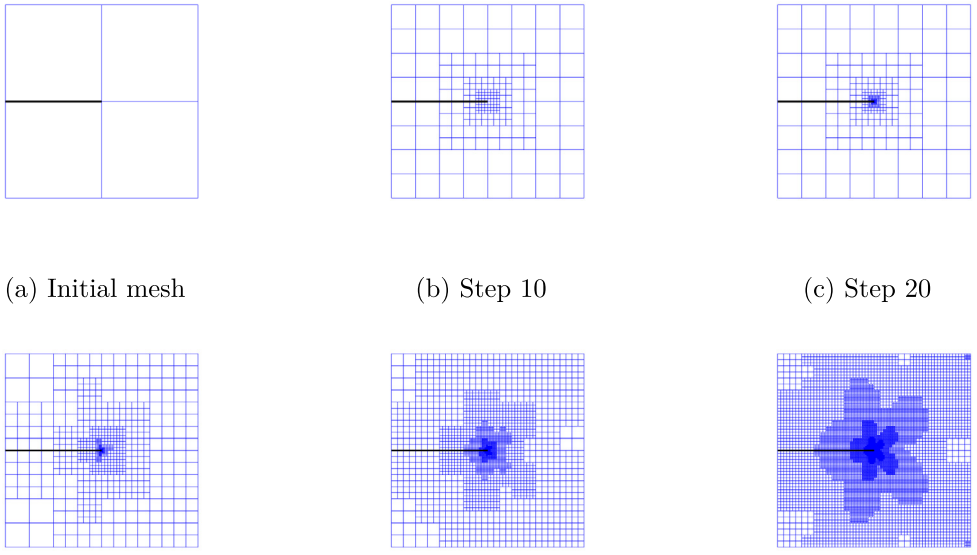

(a) Initial mesh (b) Step 10 (c) Step 20

(d) Step 25 (e) Step 30 (f) Step 35

Fig. 7. Initial and five refined meshes for the square plate with an edge crack. ($p = 3$). The black line represents the crack.

it can be observed that for the same number of DOFs, smaller error is obtained by NURBS of lower continuity. This phenomena is previously reported by De Luycker et al. [25] in the context of X–IGA applied to linear fracture mechanics. Next, it can be seen in Fig. 9a that X–GIFT and the X–IGA C^1 yield quasi-identical solutions. This is an expected result, since the solutions in these two cases are approximated by equivalent bases: uniformly refined PHT-splines and NURBS, representing linear geometry, are both equivalent to B-Splines of C^1-continuity. The

Table 2
Value of the stabilization parameters use on the Nitsche's method.

Degree	Stabilization parameters		
$p = q$	α_Θ	α_W	α_C
3	10^7	10^9	0
4	10^7	10^{11}	0
5	10^7	10^{11}	0

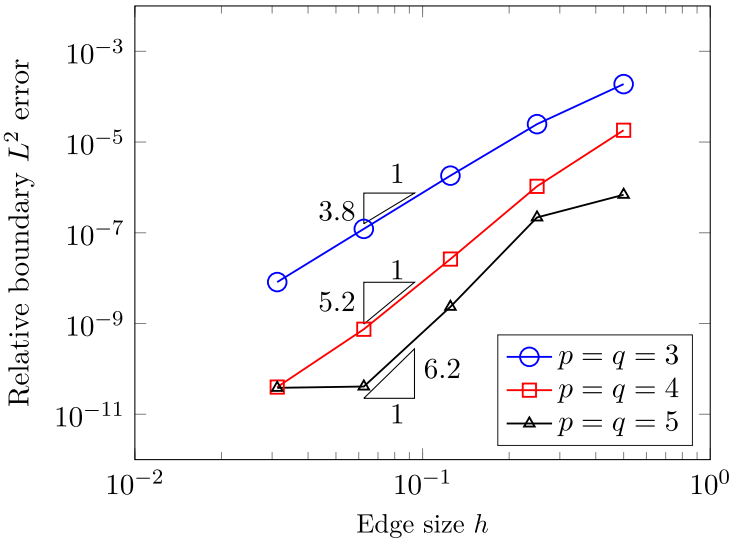

Fig. 8. Square plate with an edge crack: convergence of the boundary condition imposed by Nitsche's Method.

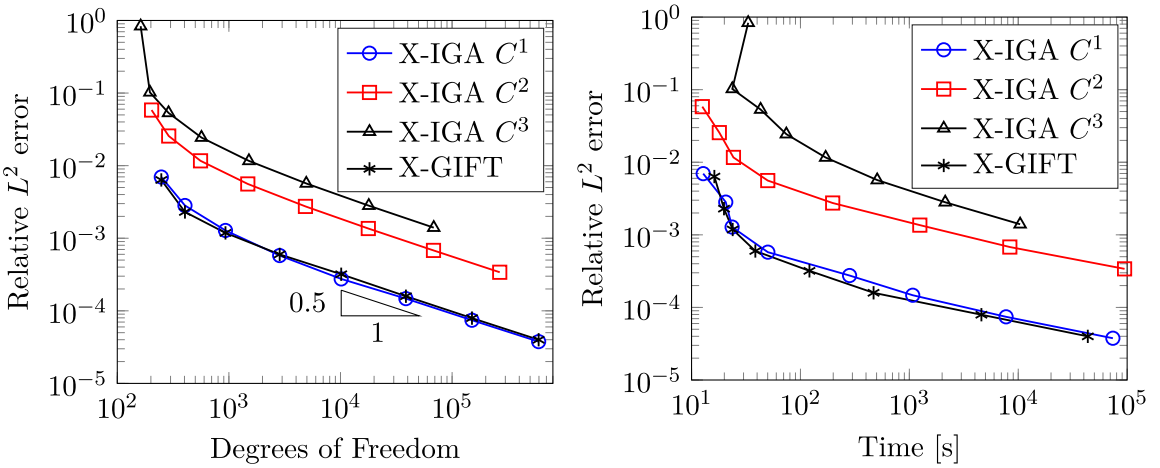

(a) L^2 error-norm vs DOF (b) L^2 error-norm vs computation time

Fig. 9. Square plate with an edge crack: convergence plots for the relative L^2 error norm versus (a) DOF and (b) time [s], for $p = 4$. Comparison between X-GIFT and X–IGA with NURBS of C^1, C^2, C^3. Different continuity is achieved by increasing knot multiplicity.

difference between these two examples is in the parameterization of the geometry. In X–GIFT, it is a coarse linear parameterization, that is kept unchanged during the solution refinement process. While in X–IGA, geometry is refined by degree elevation and knot insertion, according to the iso-parametric concept. This operation leads to

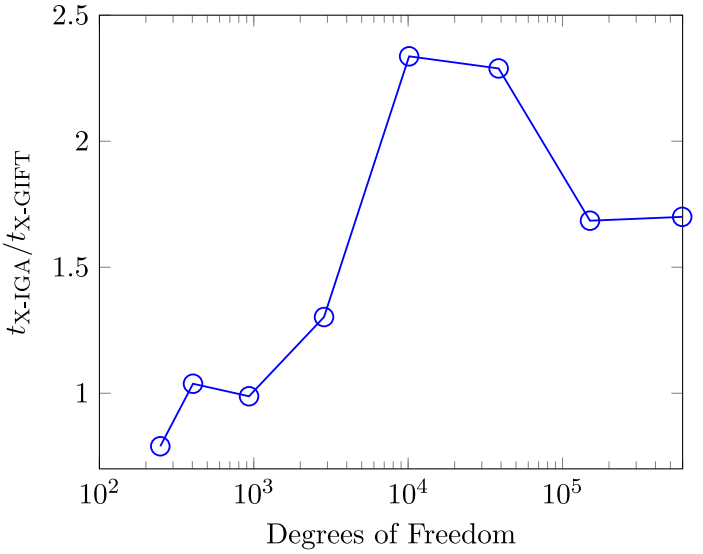

Fig. 10. Square plate with an edge crack: comparison of total computational time for X–IGA C^1 ($t_{\text{X–IGA}}$) and X–GIFT ($t_{\text{X–GIFT}}$) versus degrees of freedom.

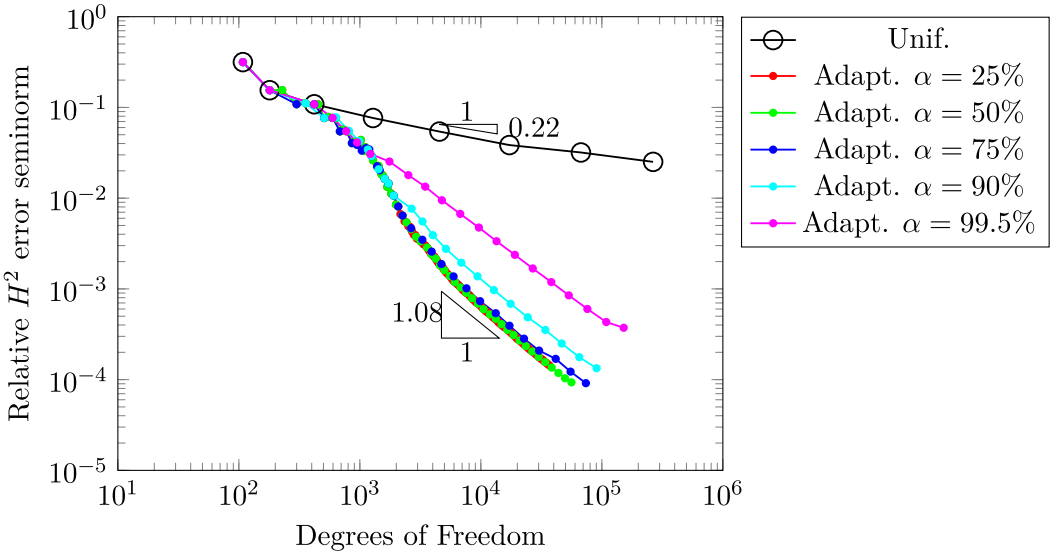

Fig. 11. Square plate with an edge crack: Study of different α parameters for the recovery-based error estimator. Relative error in H^2 semi-norm vs. the number of degrees of freedom for $p = 3$.

a noticeable difference in total computational time, as shown in Fig. 10. In this example, X–GIFT tends to be approximately 1.5 times faster compared to its X–IGA counterpart.

Fig. 9b shows that for the same level of error, splines of higher continuity require significantly more computational time.

In all remaining examples X–GIFT is employed.

Fig. 11 shows a comparison between the uniform and adaptive refinement strategies, for varying value of parameter α (percentage of the elements marked for refinement), in terms of the H^2 error semi-norm. It is interesting to note, that all marking strategies give significant improvement in the convergence rate in comparison with the uniform refinement ($\alpha = 100\%$). All other values of α lead to similar slopes, however smaller values of α lead to overall smaller error but at the price of smaller refinement steps.

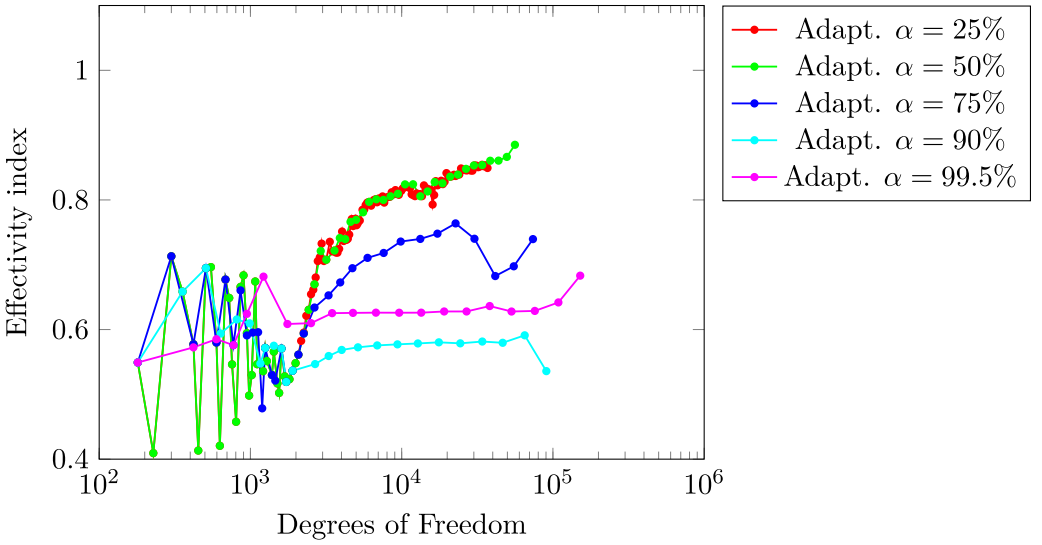

Fig. 12. Square plate with an edge crack: Study of different α parameters for the recovery-based error estimator. Effectivity index vs. the number of degrees of freedom for $p = 3$.

Table 3
Square plate with an edge crack: stress intensity factor $k2$ computed by interaction integral using different r_d radius. Exact value is $k_2 = 1$.

k_2						
$p = q$		$r_d = 2.5\overline{a}$	$r_d = 0.1$	$r_d = 0.2$	$r_d = 0.3$	$r_d = 0.4$
3	Uniform (4548 DOFs)	1.012	0.998	0.994	0.978	0.977
	Adaptive (1338 DOFs)	0.998	0.996	0.996	1.089	0.996
4	Uniform (9944 DOFs)	1.011	0.997	0.993	0.978	0.977
	Adaptive (1874 DOFs)	1.001	0.997	0.996	1.088	0.995
5	Uniform (10233 DOFs)	1.019	0.962	1.001	0.975	0.983
	Adaptive (2331 DOFs)	1.000	0.997	0.997	1.088	0.994

Fig. 12 shows the effectivity index (which is defined as the ratio between the error estimator and the error itself) computed for the recovery-based adaptive refinement for $p = 3$ and various values of α. From Fig. 12, we can conclude that smaller values of α yield the effectivity index closer to 1, which means that the error estimator tends to the H^2 error semi-norm. On the other hand, taking greater values of α leads to the effectivity index in the interval between 0.6 and 0.8. In view of this analysis, for the following examples we choose $\alpha = 75\%$, since it leads to a good balance between the computational cost and reliability of the error estimator.

Fig. 13 shows the convergence plot in relative H^2 error semi-norm (Eq. (79)) and the recovery-based error estimator given by Eq. (71) for PHT-splines of degree $p = q = 3, 4, 5$ using $\alpha = 75\%$. In all cases, the convergence rate observed for the adaptive refinement is significantly higher than their corresponding uniform refinement. For the uniform refinement, different p leads to almost the same sub-optimal convergence rate for both the H^2 error semi-norm and recovery-based error estimator. Note, that the optimal convergence rate for the H^2 error semi-norm with respect to the DOFs is $(p - 1)/2$.

Table 3 shows the stress intensity factor k_2 computed using the domain integral method (Eq. (66)) with different inner radius r_d for the domain integral. Both uniform and adaptive refinement results are presented, for $p = 3, 4, 5$. Uniform and adaptive refinement lead to similar results, with the adaptive refinement being significantly more efficient in terms of the DOFs. Choice of reducing the domain size according to $r_d = 2.5\overline{a}$, as suggested by [47,50], seems to be slightly more accurate in comparison with the fixed value.

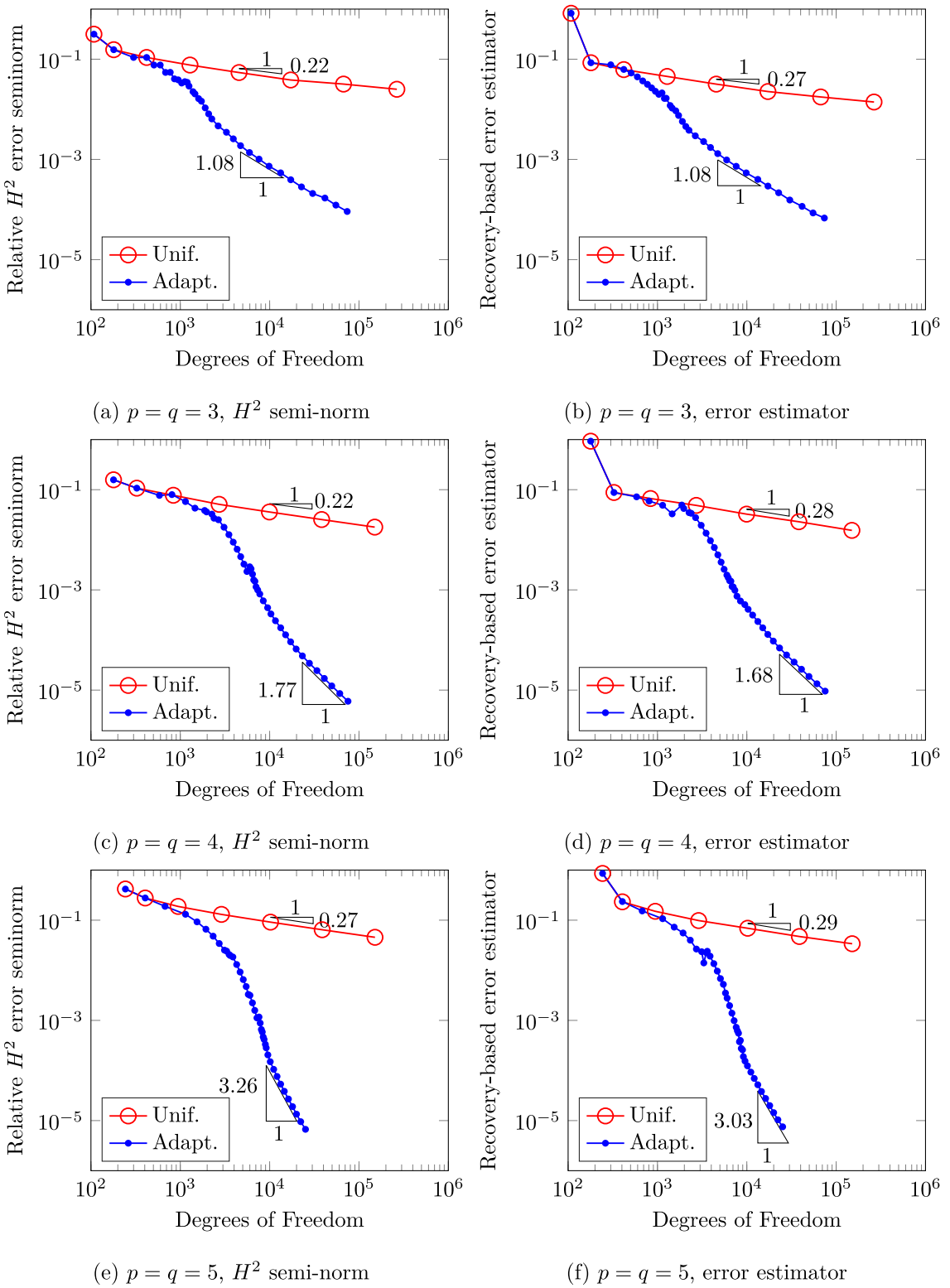

(a) $p = q = 3$, H^2 semi-norm

(b) $p = q = 3$, error estimator

(c) $p = q = 4$, H^2 semi-norm

(d) $p = q = 4$, error estimator

(e) $p = q = 5$, H^2 semi-norm

(f) $p = q = 5$, error estimator

Fig. 13. Square plate with an edge crack: rates of convergence for (a),(c),(e) H^2 semi-norm and (b),(d),(f) recovery-based error estimator, for different p. Comparison between Uniform (Unif.) and recovery-based adaptive (Adapt.) refinement.

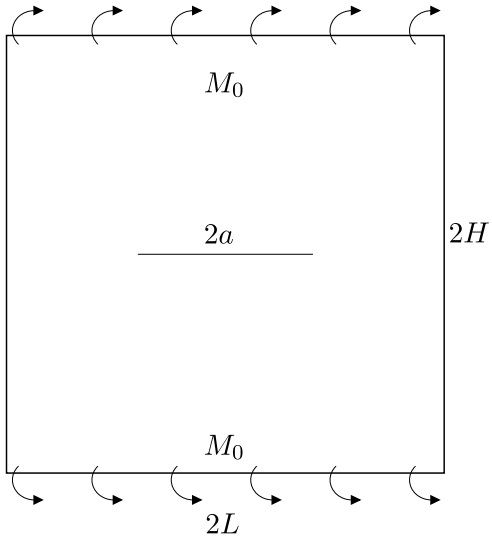

Fig. 14. Plate with center crack subjected to constant moment M_0 applied on the two edges parallel to the crack.

7.1.2. Square plate with a central crack

In the second example, as shown in Fig. 14, we consider a square plate with a central crack under constant moment loading M_0 applied on the two edges that are parallel to the crack.

The plate dimensions are taken as: length $L = 2$, width $H = 2$, thickness $h = 0.09$ and crack length $a = 1$; while the material parameters are: Young's modulus $E = 14.98$ [kPa], Poisson's ratio $\nu = 0.3$ and the constant moment loading $M_0 = 1$. This problem is also considered in [37,55]. The reference stress intensity factor are:

$$k_1 = \frac{6M_0\sqrt{a}}{h^2} \quad , \quad k_2 = 0 \tag{81}$$

Fig. 15 shows the numerical solution for the vertical displacement obtained using cubic PHT-Splines. Fig. 16 shows six different adaptive refinement steps generated using PHT-splines of degree $p = q = 3$. Similarly to the previous example, the algorithm performs gradient refinement towards the two crack tips.

Fig. 17 shows the convergence plots for the recovery-based error estimator using degree $p = q = 3, 4, 5$, for the uniform and adaptive refinement strategies. As it can be seen, the convergence rate for the adaptive refinement is significantly higher than the uniform one for all values of p.

Fig. 18 shows the normalized SIF k_1 computed for $p = 3$ for different J-integral domain radius r_d, both: fixed and dependent on the mean area of fully cracked elements ($\overline{a}$), i.e. decreasing as the mesh is refined. As it follows from Fig. 18, the optimal choices are $r_d = 0.4a$, $r_d = 0.5a$, $r_d \geq 3.0\overline{a}$.

Fig. 19 shows the convergence of the normalized stress intensity factor k_1 to the reference solution, for different degrees of polynomial $p = q = 3, 4, 5$, using $r_d = 0.4a$. It can be seen that the adaptive refinement procedure yields more accurate results with less DOFs.

7.1.3. Square plate with a central crack subjected to constant pressure

The following example includes a square plate with a central crack under uniform pressure $p = 1$ applied on the top of the plate. The plate is simply supported at all boundaries. This problem is also considered in [35] in the context of thin shell theory and in [47,50] in the context of phantom node method.

The plate dimensions are: length $L = 1$, width $H = 1$, thickness $h = 0.1$ and crack length $a = 0.8$; while the material parameters are: Young's Modulus $E = 1000$ and Poisson's ratio $\nu = 0.3$ (see Fig. 20).

Fig. 21 shows the deformed shape of the plate using the numerical solution with PHT-Splines $p = q = 3$. Fig. 22 shows the convergence plots for the recovery-based error estimator using uniform and adaptive refinement with PHT-Splines of degree $p = q = 3, 4, 5$. Again, as observed in the previous two examples, the convergence rate of the adaptive refinement is significantly higher in comparison with the uniform one.

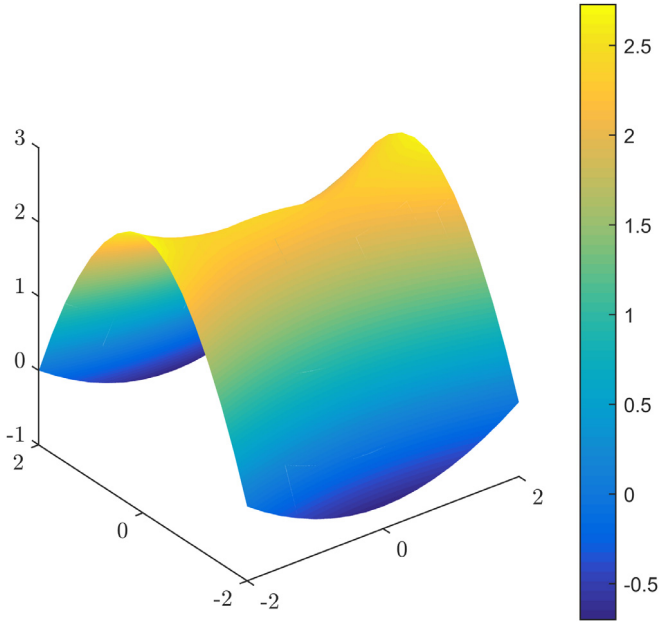

Fig. 15. Numerical solution for the square plate with a center crack subject to constant moment.

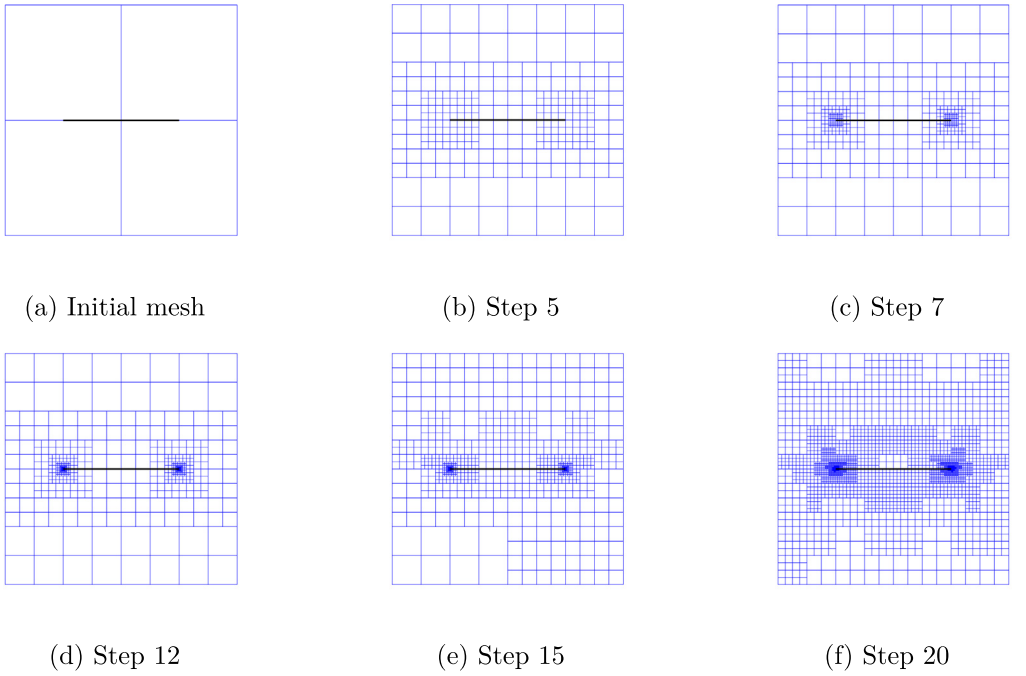

(a) Initial mesh (b) Step 5 (c) Step 7

(d) Step 12 (e) Step 15 (f) Step 20

Fig. 16. Initial and refined meshes for the plate with central crack. PHT-Splines of degree $p = q = 3$. The black line represents the crack.

Fig. 23 shows the convergence plot of the J-integral (Eq. (62)) for $p = q = 3$ using uniform and adaptive refinement with $r_d = 0.2a$. The results are also compared with the results reported in [35,47,50,56] for several numerical methods. Both uniform and adaptive refinement results are in a good agreement with the reference results, however for given values of parameters, the uniform refinement slightly outperforms the adaptive one.

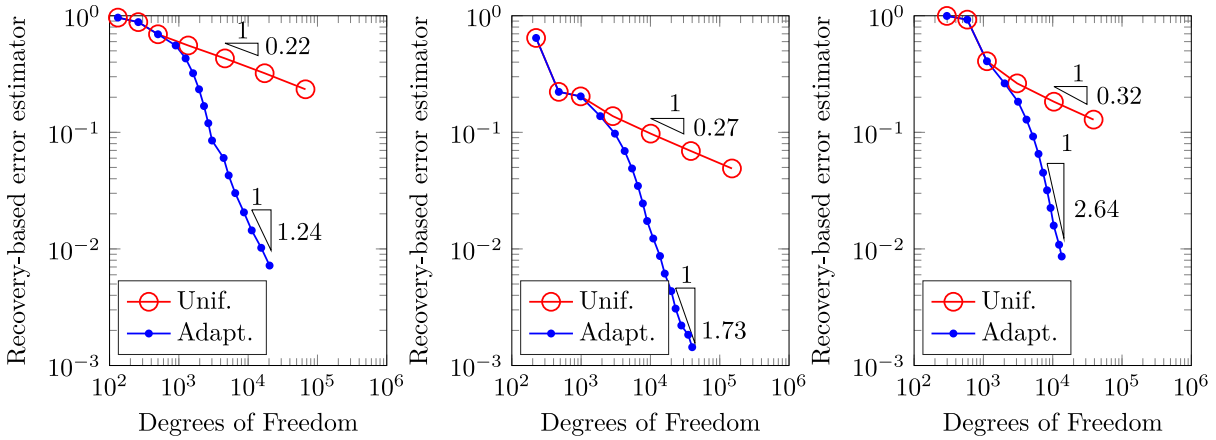

(a) $p = q = 3$. (b) $p = q = 4$. (c) $p = q = 5$.

Fig. 17. Square plate with center crack under constant moments: Convergence of recovery-based error estimator for degrees 3, 4 and 5. Comparison between Uniform (Unif.) and recovery-based adaptive (Adapt.) refinement.

Table 4
Normalized natural frequencies of a simply supported plate with a central crack of crack ratio $a/L = 0.4$.

Method	Degree	Modes					
		1	2	3	4	5	6
PHT-splines X-GIFT	3	18.287	46.633	49.034	78.612	85.493	98.604
	4	18.290	46.629	49.043	78.610	85.497	98.600
	5	18.283	46.623	49.031	78.609	85.490	98.599
Ref. [57]		18.281	46.533	49.028	78.579	85.414	98.678
Ref. [58]		18.28	45.84	49.02	78.41	84.96	98.65
Ref. [59]		18.28	46.62	49.03	78.60	85.51	98.68

7.2. Vibration of plates with cracks

7.2.1. Square plate with a central crack

We perform the vibration analysis of the plate of the same geometry as in the previous example. In this example, the material parameters are: Young's Modulus $E = 2e11$, Poisson's ratio $\nu = 0.3$ and density $\rho = 6000$. The plate dimensions are taken as: $L = H = 5$ and the thickness $h = 0.1$. The crack length a is kept variable to study the influence of the crack length on the natural modes.

The natural frequencies ω are normalized as:

$$\overline{\omega} = \omega L^2 \sqrt{\frac{\rho h}{D}} \tag{82}$$

Fig. 24 shows the convergence plot for the first three vibration modes, $p = 3, 4, 5$ and $a/L = 0.4$ in terms of natural frequencies. For each mode, the reference values are also included. Tables 4 and 5 show the normalized natural frequencies $\overline{\omega}$ obtained for the first six natural modes, using PHT-splines of degree $p = q = 3, 4, 5$ and crack ratio of a/L equal to 0.4 and 0.8, respectively. The results are also compared with the data available in the literature. In both cases ($a/L = 0.4$ and 0.8) the results obtained for different degrees p agree well with the reference solutions. Fig. 25 shows the first six modes for a simply supported square plate with a crack ratio of $a/L = 0.4$.

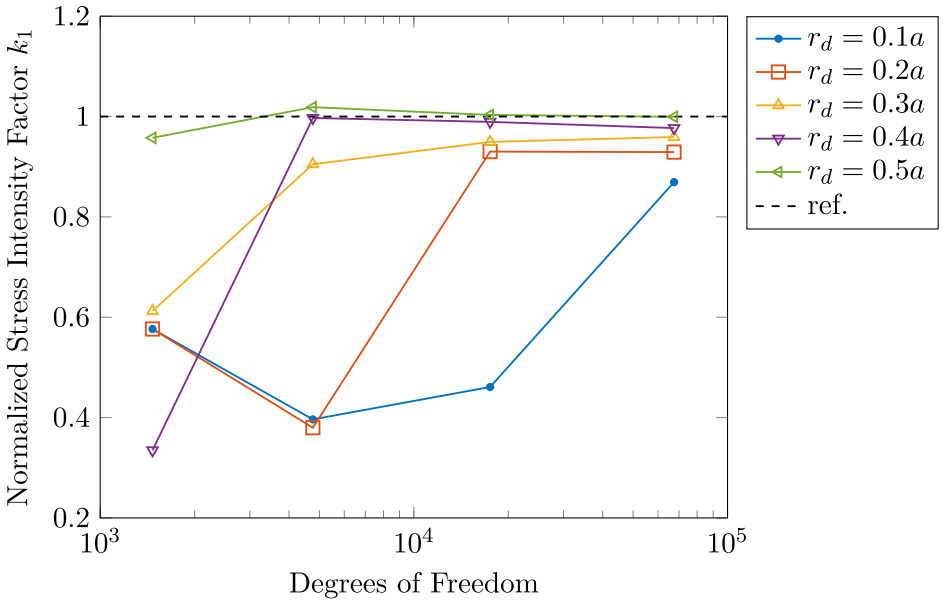

(a) r_d fixed

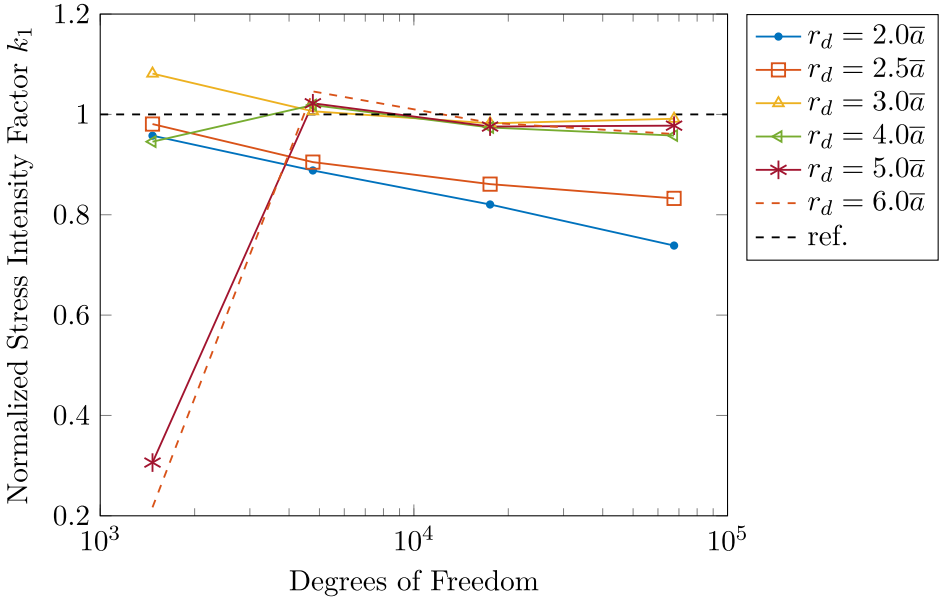

(b) r_d shrinking

Fig. 18. Square plate with center crack under constant moments: Comparison between different J-integral domain radius r_d for the computation of the normalized SIF k_1; $p = 3$ and uniform refinement.

7.2.2. Clamped circular plate with a central crack

In this problem, the numerical results of the vibration analysis for a circular plate with a central crack are presented. The plate has a radius R, thickness $h = R/2$ and a crack of length $2a$. The plate is fully clamped (see Fig. 26). The material parameters are: Young's Modulus $E = 70e9$, Poisson's ratio $\nu = 0.3$ and density $\rho = 2707$.

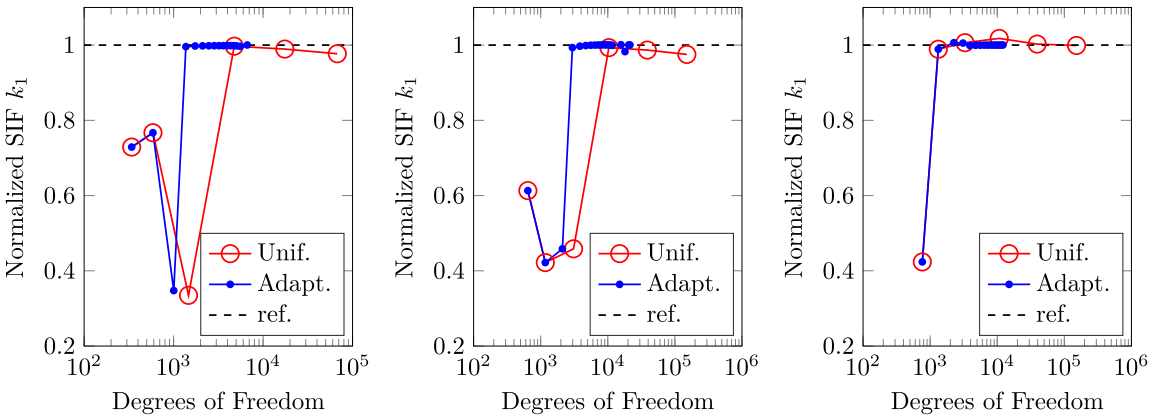

Fig. 19. Square plate with center crack under constant moments: Normalized stress intensity factor k_1 for degrees 3, 4 and 5. Comparison between uniform (Unif.) and recovery-based adaptive (Adapt.) refinement. Theoretical value is presented in the dashed line.

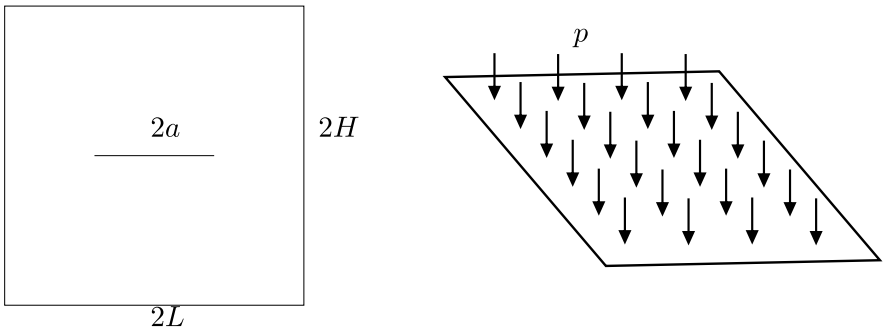

Fig. 20. Plate with center crack subjected to a constant distributed load p applied on the top surface of the plate.

Table 5
Normalized natural frequencies of a simply supported plate with a central crack of crack ratio $a/L = 0.8$.

Method	Degree	Modes					
		1	2	3	4	5	6
PHT-splines X-GIFT	3	16.408	27.765	47.203	65.743	76.359	78.382
	4	16.407	27.761	47.202	65.738	76.359	78.379
	5	16.423	27.760	47.186	65.733	76.360	78.363
Ref. [57]		16.401	27.743	47.255	65.587	76.371	78.256
Ref. [58]		16.40	26.71	47.23	64.39	76.36	77.96
Ref. [59]		16.40	27.77	47.26	65.73	76.37	78.38

The information necessary to generate the circular geometry with NURBS is presented in Table A.8. In this example, the normalized natural frequencies are defined as:

$$\overline{\omega} = \omega \frac{R^2}{h} \sqrt{\frac{\rho}{E}} \tag{83}$$

Fig. 27 shows the convergence plot of the first natural frequency, using uniform and adaptive refinement, with $p = 3, 4, 5$. Table 6 shows the normalized natural frequencies obtained for the first six natural modes, using PHT-splines of degree $p = q = 3, 4, 5$ and crack ratio of a/R equal to 0.25 and 0.5, respectively.

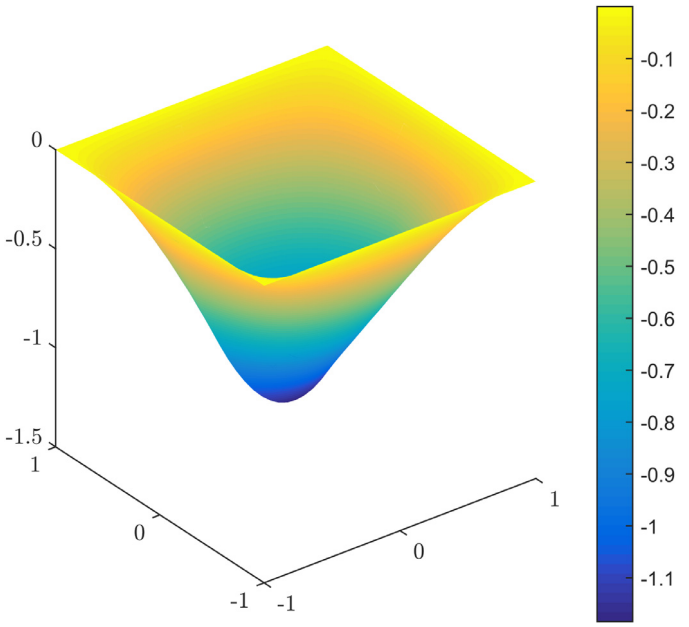

Fig. 21. Numerical solution for the vertical displacement of the square plate with a straight crack subject to constant distributed loading, $a/L = 0.4$.

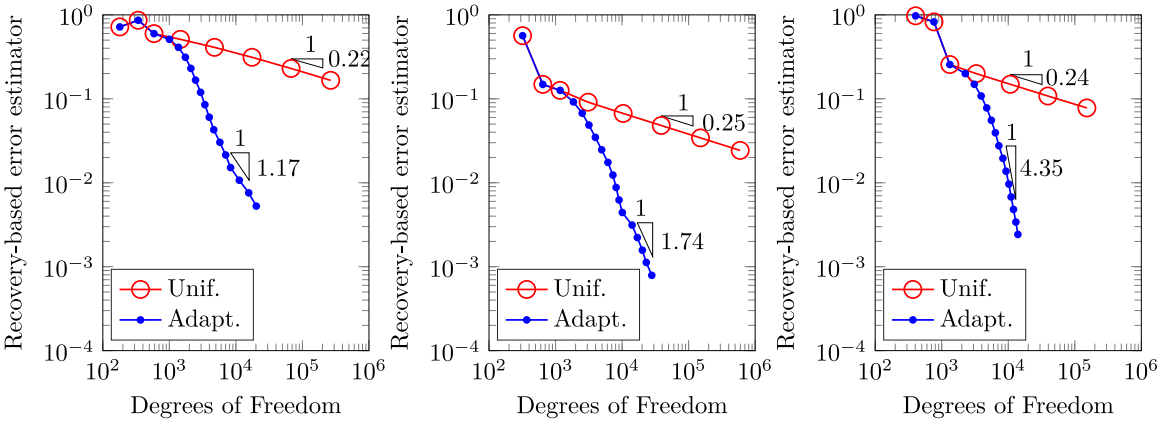

(a) $p = q = 3$. (b) $p = q = 4$. (c) $p = q = 5$.

Fig. 22. Constant pressure loading problem: Convergence plot of recovery-based error estimator for degrees 3, 4 and 5. Comparison between uniform (Unif.) and recovery-based adaptive (Adapt.) refinement.

Fig. 28 shows the first six modes for a clamped circular plate with a crack size $a/R = 0.25$.

7.2.3. Clamped annular plate with two symmetric cracks

In this section, the numerical results of the vibration analysis for an annular plate with two symmetric cracks emanating from the inner edge are presented. The plate has internal radius r, external radius R and two symmetric cracks of length $a = 0.1$. The plate is clamped in the exterior radius, while the internal radius is free, as it can be seen in Fig. 29. The material parameters are: Young's Modulus $E = 70e9$, Poisson's ratio $\nu = 0.3$ and density $\rho = 2707$.

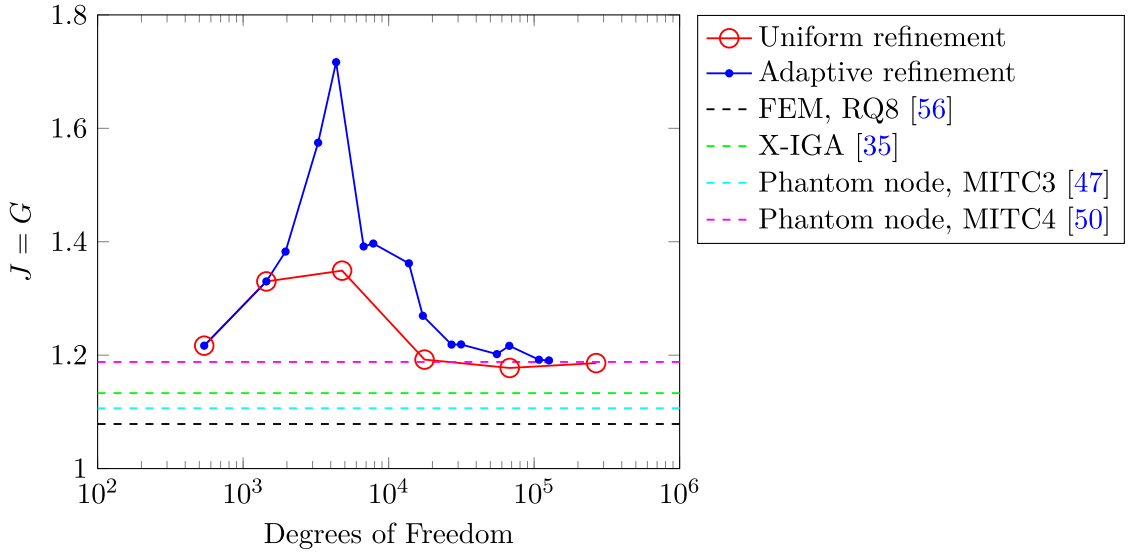

Fig. 23. Square plate under constant pressure: Convergence plot for the J-integral; $p = 3$ and $a/L = 0.8$.

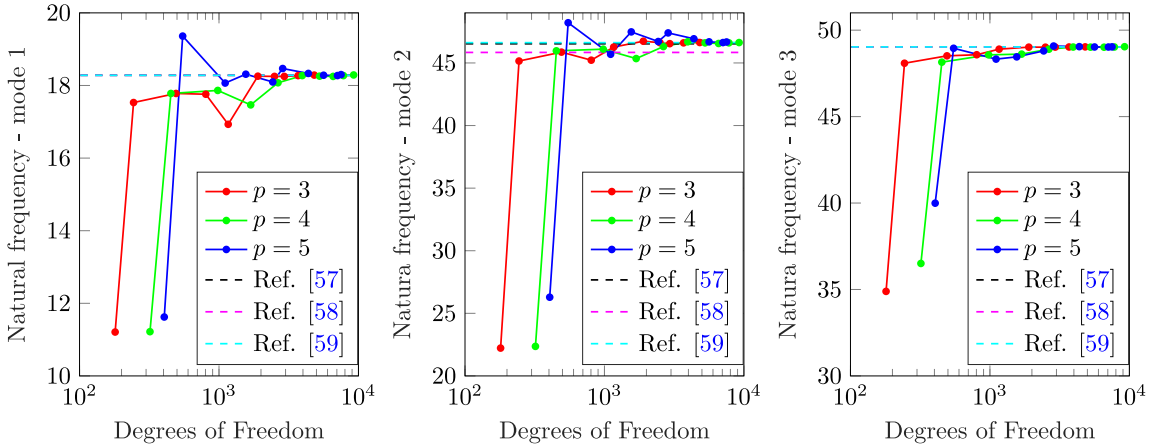

(a) Mode 1 (b) Mode 2 (c) Mode 3

Fig. 24. Square plate with a central crack problem: Convergence plot of the first three vibration modes. Adaptive (Adapt.) refinement using $p = 3, 4, 5$. $a/L = 0.4$.

Table 6
Normalized natural frequencies for a simply supported circular plate with a central crack.

a/R	Degree	DOFs	Mode					
			1	2	3	4	5	6
0.25	3	9 552	3.467	6.911	7.071	10.700	11.588	12.059
	4	10 796	3.494	6.910	7.071	10.698	11.588	12.061
	5	11 394	3.486	6.902	7.066	10.679	11.587	12.048
0.5	3	14 956	3.296	5.102	6.808	9.860	10.685	10.865
	4	12 060	3.280	5.098	6.837	9.846	10.683	10.864
	5	12 150	3.319	5.082	6.873	9.836	10.673	10.852

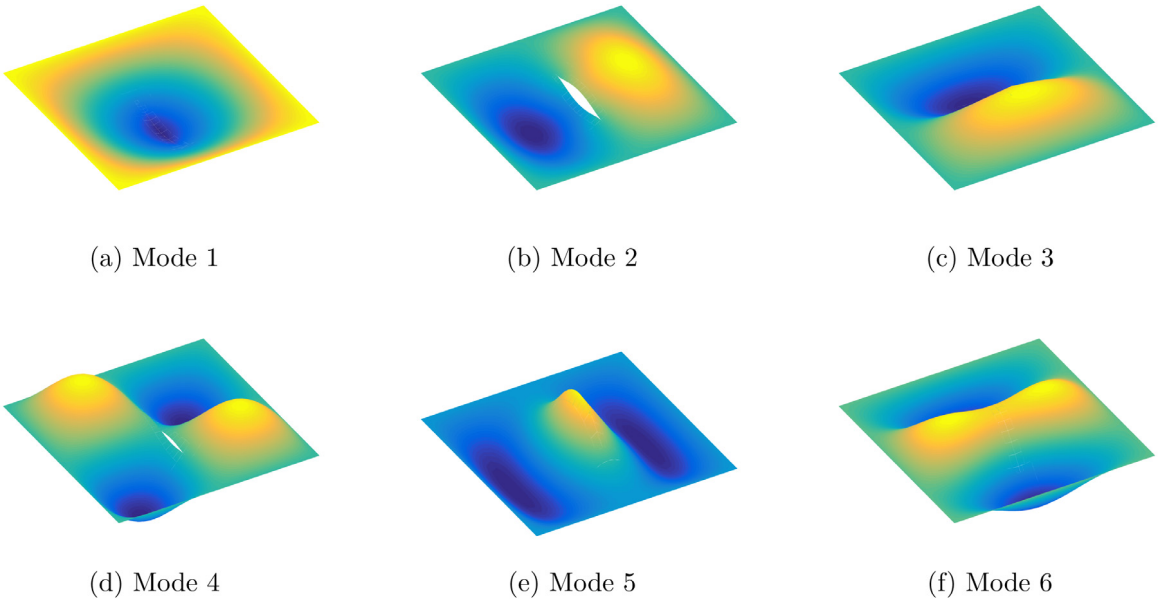

Fig. 25. The first six vibration mode shape for a simply supported square plate with a crack ratio of $a/L = 0.4$.

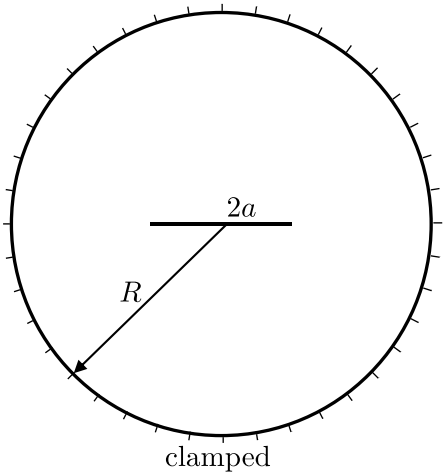

Fig. 26. Circular plate with center crack.

The information necessary to generate the annular geometry are presented in Table A.9. The geometry is parameterized by four symmetric NURBS of degrees 1 and 2. Note, that in this example C^0-continuity between patches is imposed by matching corresponding degrees of freedom on the patch boundaries, as discussed in [60].

The normalized natural frequencies are defined as

$$\overline{\omega} = \omega \frac{(R-r)^2}{h}\sqrt{\frac{\rho}{E}} \tag{84}$$

Table 7 shows the normalized natural frequencies obtained for the first six natural modes, using PHT-splines of degree $p = q = 3$ and $r/R = 0.6$.

Fig. 30 shows the first six modes for a clamped annular plate with a radius ratio of $r/R = 0.8$.

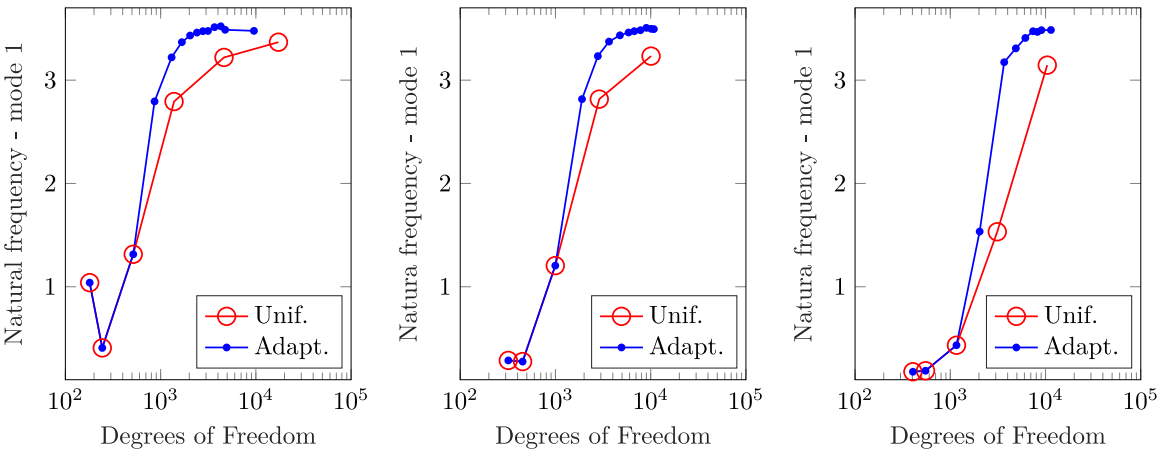

(a) $p = 3$ (b) $p = 4$ (c) $p = 5$

Fig. 27. Circular plate with a crack: Convergence plot of the first vibration mode. Comparison between uniform (Unif.) and adaptive (Adapt.) refinement using $p = 3, 4, 5$ and a crack ratio of $a/R = 0.25$.

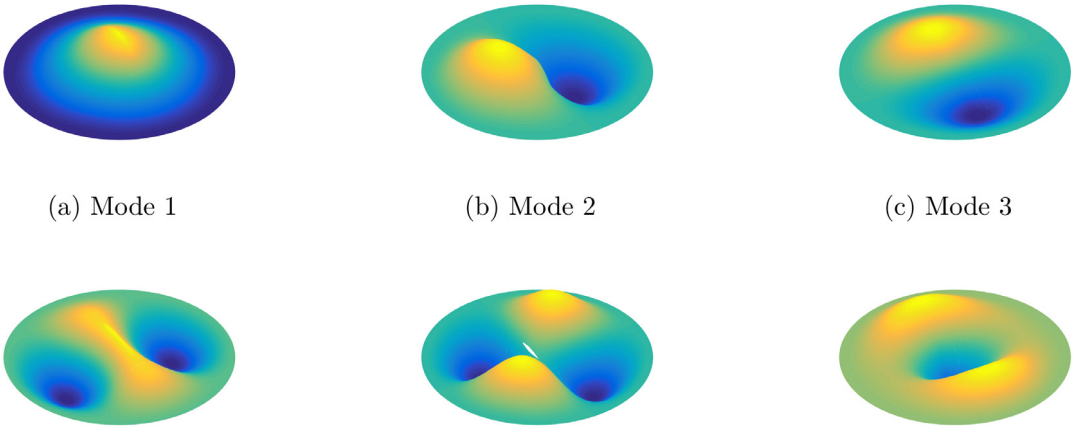

(a) Mode 1 (b) Mode 2 (c) Mode 3

(d) Mode 4 (e) Mode 5 (f) Mode 6

Fig. 28. The first six vibration mode shapes for the circular plate with a center crack with $R = 10$ and crack length $a = 2.5$.

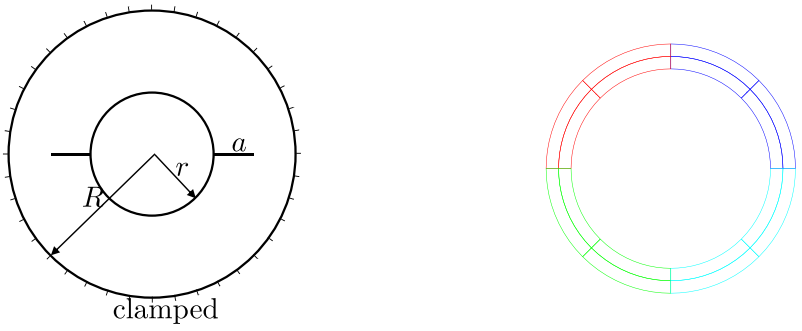

(a) Problem domain. (b) NURBS patches.

Fig. 29. Annular plate with two symmetric cracks: Problem domain and NURBS patches.

Table 7
Normalized natural frequencies for a clamped annular plate with two symmetric cracks, $p = q = 3, 4, 5$, $r/R = 0.6$.

Degree	DOFs	Mode					
		1	2	3	4	5	6
3	8 844	1.242	1.259	1.359	1.480	1.506	1.782
4	9 002	1.242	1.259	1.359	1.480	1.506	1.783
5	10 582	1.236	1.270	1.360	1.474	1.507	1.783

Table A.8
Geometry information for the circular geometry.

Patch	Knot vector		Control points		
	U	V	x	y	w
1	[0,0,0,1,1,1]	[0,0,0,1,1,1]	$-R\frac{\sqrt{2}}{2}$	$R\frac{\sqrt{2}}{2}$	1
			$-R\sqrt{2}$	0	$\frac{\sqrt{2}}{2}$
			$-R\frac{\sqrt{2}}{2}$	$-R\frac{\sqrt{2}}{2}$	1
			0	$R\sqrt{2}$	$\frac{\sqrt{2}}{2}$
			0	0	1
			0	$-R\sqrt{2}$	$\frac{\sqrt{2}}{2}$
			$R\frac{\sqrt{2}}{2}$	$R\frac{\sqrt{2}}{2}$	1
			$R\sqrt{2}$	0	$\frac{\sqrt{2}}{2}$
			$R\frac{\sqrt{2}}{2}$	$-R\frac{\sqrt{2}}{2}$	1

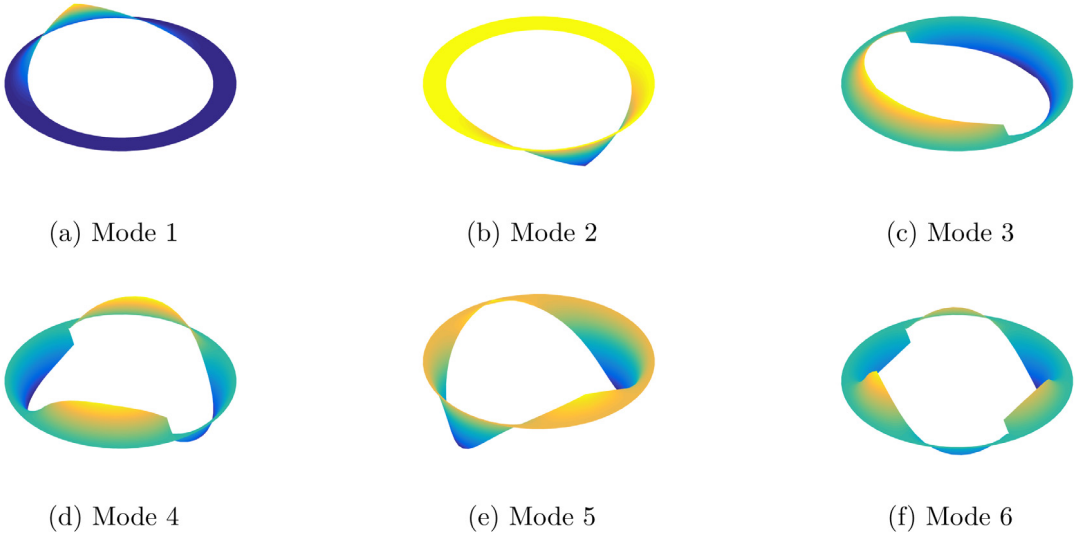

Fig. 30. The first six vibration mode shapes for the clamped annular plate with two symmetric cracks with $R = 1$, $r = 0.8$ and crack length $a = 0.1$.

8. Conclusions

In this work, we show the application of PHT-splines in the framework of eXtended Geometry Independent Field approximaTion (X–GIFT) for problems of bending and vibration of cracked Kirchhoff–Love plates. In this formulation, the original coarse NURBS parameterization of the plate geometry is paired with a PHT-splines approximation of the solution, enriched by the Heaviside function and crack tip asymptotic expansions. The enriched

Table A.9
Geometry information for the annular geometry.

Patch	Knot vector		Control points		
	U	V	x	y	w
1	[0,0,1,1]	[0,0,0,1,1,1]	r	0	1
			$r\frac{\sqrt{2}}{2}$	$r\frac{\sqrt{2}}{2}$	$\frac{\sqrt{2}}{2}$
			0	r	1
			R	0	1
			$R\frac{\sqrt{2}}{2}$	$R\frac{\sqrt{2}}{2}$	$\frac{\sqrt{2}}{2}$
			0	R	1
2	[0,0,1,1]	[0,0,0,1,1,1]	0	r	1
			$-r\frac{\sqrt{2}}{2}$	$r\frac{\sqrt{2}}{2}$	$\frac{\sqrt{2}}{2}$
			$-r$	0	1
			0	R	1
			$-R\frac{\sqrt{2}}{2}$	$R\frac{\sqrt{2}}{2}$	$\frac{\sqrt{2}}{2}$
			$-R$	0	1
3	[0,0,1,1]	[0,0,0,1,1,1]	r	0	1
			$-r\frac{\sqrt{2}}{2}$	$-r\frac{\sqrt{2}}{2}$	$\frac{\sqrt{2}}{2}$
			0	$-r$	1
			$-R$	0	1
			$-R\frac{\sqrt{2}}{2}$	$-R\frac{\sqrt{2}}{2}$	$\frac{\sqrt{2}}{2}$
			0	$-R$	1
4	[0,0,1,1]	[0,0,0,1,1,1]	0	$-r$	1
			$r\frac{\sqrt{2}}{2}$	$-r\frac{\sqrt{2}}{2}$	$\frac{\sqrt{2}}{2}$
			r	0	1
			0	$-R$	1
			$R\frac{\sqrt{2}}{2}$	$-R\frac{\sqrt{2}}{2}$	$\frac{\sqrt{2}}{2}$
			R	0	1

solution is adaptively refined using a recovery-based error estimator, while the NURBS parameterization of the geometry remains unchanged. The main results are summarized below:

- This work serves as a proof of concept of GIFT, introduced in [15]. The approach enables to relax tight coupling between the geometry and solution bases in standard IGA, i.e. the requirement of iso-parametric approximation. In [15], GIFT was applied to problems of heat conduction and linear elasticity, in [18] - to time-harmonic acoustics, where it was shown that NURBS geometry and PHT-splines as solution basis yield optimal convergence rate and lead to computational savings in comparison with NURBS-based IGA and PHT-splines based IGA. Computational savings are associated with avoiding geometry refinement and utilizing adaptive local refinement of the solution. All features of GIFT reported earlier, are observed in the present work in the framework of Kirchhoff–Love plate theory. Moreover, it is shown that the solution approximation can be further enriched to accommodate a crack.
- Numerical results in terms of stress intensity factors, natural frequencies and L^2 and H^2-errors are compared with analytical solutions and data, obtained by other methods, and shown to be highly accurate.
- Numerical results are compared with X–IGA with NURBS of different continuity and it is shown that the basis of lower continuity yields lower error per degree of freedom. Moreover, X–GIFT is estimated to be about 1.5 faster than X–IGA with C^1-continuity due to avoiding geometry refinement.
- The proposed recovery-based error estimator is based on the energy norm for the Kirchhoff–Love plate. This error estimator drives adaptive refinement towards the crack-face and crack tips, improving the overall convergence rate of the solution and accuracy of the fracture parameters evaluation.
- Adaptive refinement also allows computing vibration modes with fewer DOFs compared to a uniform refinement. Various strategies are discussed for enrichment, refinement, and computation of SIFs and J-integrals.

Acknowledgments

Elena Atroshchenko, Felipe Contreras and Javier Videla are partly supported by CONICYT grant REDI170090. Javier Videla thanks CONICYT for funding from MSc fellowship 22171388. The authors also thank Prof. Stéphane Bordas and Legato Team (https://legato-team.eu/) for fruitful discussions and use of the HPC facilities.

Appendix. Geometry parameterization employed in the numerical examples

See Tables A.8 and A.9

References

[1] A.E.H. Love, The small free vibrations and deformation of a thin elastic shell, Philos. Trans. R. Soc. Lond. A 179 (1888) 491–546.
[2] T. Hughes, J. Cottrell, Y. Bazilevs, Isogeometric analysis: CAD, finite elements, NURBS, exact geometry and mesh refinement, Comput. Methods Appl. Mech. Engrg. 194 (39–41) (2005) 4135–4195.
[3] T.W. Sederberg, J. Zheng, A. Bakenov, A. Nasri, T-splines and T-NURCCs, ACM Trans. Graph. 22 (3) (2003) 477–484.
[4] Y. Bazilevs, V.M. Calo, J.A. Cottrell, J.A. Evans, T.J.R. Hughes, S. Lipton, M.A. Scott, T.W. Sederberg, Isogeometric analysis using T-splines, Comput. Methods Appl. Mech. Engrg. 199 (5) (2010) 229–263.
[5] M.R. Dörfel, B. Jüttler, B. Simeon, Adaptive isogeometric analysis by local h-refinement with T-splines, Comput. Methods Appl. Mech. Engrg. 199 (5) (2010) 264–275.
[6] M.A. Scott, M.J. Borden, C.V. Verhoosel, T.W. Sederberg, T.J. Hughes, Isogeometric finite element data structures based on Bézier extraction of T-splines, Internat. J. Numer. Methods Engrg. 88 (2) (2011) 126–156.
[7] M.A. Scott, X. Li, T.W. Sederberg, T.J.R. Hughes, Local refinement of analysis-suitable T-splines, Comput. Methods Appl. Mech. Engrg. 213–216 (2012) 206–222.
[8] A. Buffa, D. Cho, G. Sangalli, Linear independence of the T-spline blending functions associated with some particular T-meshes, Comput. Methods Appl. Mech. Engrg. 199 (23) (2010) 1437–1445.
[9] N. Nguyen-Thanh, H. Nguyen-Xuan, S.P.A. Bordas, T. Rabczuk, Isogeometric analysis using polynomial splines over hierarchical T-meshes for two-dimensional elastic solids, Comput. Methods Appl. Mech. Engrg. 200 (21–22) (2011) 1892–1908.
[10] J. Deng, F. Chen, X. Li, C. Hu, W. Tong, Z. Yang, Y. Feng, Polynomial splines over hierarchical T-meshes, Graph. Models 70 (4) (2008) 76–86.
[11] N. Nguyen-Thanh, K. Zhou, Extended isogeometric analysis based on PHT-splines for crack propagation near inclusions, Internat. J. Numer. Methods Engrg. 112 (12) (2017) 1777–1800.
[12] C. Anitescu, M.N. Hossain, T. Rabczuk, Recovery-based error estimation and adaptivity using high-order splines over hierarchical T-meshes, Comput. Methods Appl. Mech. Engrg. 328 (2018) 638–662.
[13] L. Chen, R. de Borst, Locally refined T-splines, Internat. J. Numer. Methods Engrg. 114 (6) (2018) 637–659.
[14] B. Marussig, J. Zechner, G. Beer, T.-P. Fries, Fast isogeometric boundary element method based on independent field approximation, Comput. Methods Appl. Mech. Engrg. 284 (2015) 458–488.
[15] E. Atroshchenko, S. Tomar, G. Xu, S. Bordas, Weakening the tight coupling between geometry and simulation in isogeometric analysis: From sub-and super-geometric analysis to Geometry-Independent Field approximation (GIFT), Internat. J. Numer. Methods Engrg. 114 (10) (2018) 1131–1159.
[16] P. Yu, C. Anitescu, S. Tomar, S.P.A. Bordas, P. Kerfriden, Adaptive isogeometric analysis for plate vibrations: An efficient approach of local refinement based on hierarchical a posteriori error estimation, Comput. Methods Appl. Mech. Engrg. 342 (2018) 251–286.
[17] L.B. Da Veiga, A. Buffa, C. Lovadina, M. Martinelli, G. Sangalli, An isogeometric method for the Reissner–Mindlin plate bending problem, Comput. Methods Appl. Mech. Engrg. 209 (2012) 45–53.
[18] J. Videla, C. Anitescu, T. Khajah, S.P. Bordas, E. Atroshchenko, H-and p-adaptivity driven by recovery and residual-based error estimators for PHT-splines applied to time-harmonic acoustics, Comput. Math. Appl. 77 (9) (2019) 2369–2395.
[19] I. Babuvška, W.C. Rheinboldt, Error estimates for adaptive finite element computations, SIAM J. Numer. Anal. 15 (4) (1978) 736–754.
[20] O. Zienkiewicz, J. Zhu, The superconvergent patch recovery and a posteriori error estimates. Part 1: The recovery technique, Internat. J. Numer. Methods Engrg. 33 (7) (1992) 1331–1364.
[21] O. Zienkiewicz, J. Zhu, The superconvergent patch recovery and *a posteriori* error estimates. Part 2: Error estimates and adaptivity, Internat. J. Numer. Methods Engrg. 33 (7) (1992) 1365–1382.
[22] M. Kumar, T. Kvamsdal, K.A. Johannessen, Superconvergent patch recovery and a posteriori error estimation technique in adaptive isogeometric analysis, Comput. Methods Appl. Mech. Engrg. 316 (2017) 1086–1156.
[23] N. Moës, J. Dolbow, T. Belytschko, A finite element method for crack growth without remeshing, Internat. J. Numer. Methods Engrg. 46 (1) (1999) 131–150.
[24] D.J. Benson, Y. Bazilevs, E. De Luycker, M.-C. Hsu, M. Scott, T. Hughes, T. Belytschko, A generalized finite element formulation for arbitrary basis functions: from isogeometric analysis to XFEM, Internat. J. Numer. Methods Engrg. 83 (6) (2010) 765–785.
[25] E. De Luycker, D.J. Benson, T. Belytschko, Y. Bazilevs, M.C. Hsu, X-FEM in isogeometric analysis for linear fracture mechanics, Internat. J. Numer. Methods Engrg. 87 (6) (2011) 541–565.
[26] S.S. Ghorashi, N. Valizadeh, S. Mohammadi, Extended isogeometric analysis for simulation of stationary and propagating cracks, Internat. J. Numer. Methods Engrg. 89 (9) (2012) 1069–1101.

[27] X. Peng, E. Atroshchenko, P. Kerfriden, S. Bordas, Isogeometric boundary element methods for three dimensional static fracture and fatigue crack growth, Comput. Methods Appl. Mech. Engrg. 316 (2017) 151–185.
[28] N. Nguyen-Thanh, J. Huang, K. Zhou, An isogeometric-meshfree coupling approach for analysis of cracks, Internat. J. Numer. Methods Engrg. 113 (10) (2018) 1630–1651.
[29] S. Singh, I. Singh, B. Mishra, G. Bhardwaj, T. Bui, A simple, efficient and accurate Bézier extraction based T-spline XIGA for crack simulations, Theor. Appl. Fract. Mech. 88 (2017) 74–96.
[30] S. Singh, I. Singh, G. Bhardwaj, B. Mishra, A Bézier extraction based XIGA approach for three-dimensional crack simulations, Adv. Eng. Softw. 125 (2018) 55–93.
[31] J. Dolbow, N. Moës, T. Belytschko, Modeling fracture in Mindlin–Reissner plates with the extended finite element method, Int. J. Solids Struct. 37 (48–50) (2000) 7161–7183.
[32] C. Xing, Y. Wang, H. Waisman, Fracture analysis of cracked thin-walled structures using a high-order XFEM and Irwin's integral, Comput. Struct. 212 (2019) 1–19.
[33] P.M. Areias, T. Belytschko, Non-linear analysis of shells with arbitrary evolving cracks using XFEM, Internat. J. Numer. Methods Engrg. 62 (3) (2005) 384–415.
[34] H. Bayesteh, S. Mohammadi, XFEM fracture analysis of shells: the effect of crack tip enrichments, Comput. Mater. Sci. 50 (10) (2011) 2793–2813.
[35] N. Nguyen-Thanh, N. Valizadeh, M. Nguyen, H. Nguyen-Xuan, X. Zhuang, P. Areias, G. Zi, Y. Bazilevs, L. De Lorenzis, T. Rabczuk, An extended isogeometric thin shell analysis based on Kirchhoff–Love theory, Comput. Methods Appl. Mech. Engrg. 284 (2015) 265–291.
[36] J. Lasry, J. Pommier, Y. Renard, M. Salaün, Extended finite element methods for thin cracked plates with Kirchhoff–Love theory, Internat. J. Numer. Methods Engrg. 84 (9) (2010) 1115–1138.
[37] J. Lasry, Y. Renard, M. Salaün, Stress intensity factors computation for bending plates with extended finite element method, Internat. J. Numer. Methods Engrg. 91 (9) (2012) 909–928.
[38] K.D. Nguyen, H. Nguyen-Xuan, An isogeometric finite element approach for three-dimensional static and dynamic analysis of functionally graded material plate structures, Compos. Struct. 132 (2015) 423–439.
[39] I. Harari, E. Shavelzon, Embedded kinematic boundary conditions for thin plate bending by Nitsche's approach, Internat. J. Numer. Methods Engrg. 92 (1) (2012) 99–114.
[40] S. Shojaee, E. Izadpanah, N. Valizadeh, J. Kiendl, Free vibration analysis of thin plates by using a NURBS-based isogeometric approach, Finite Elem. Anal. Des. 61 (2012) 23–34.
[41] R.G. Anderson, B. Irons, O. Zienkiewicz, Vibration and stability of plates using finite elements, Int. J. Solids Struct. 4 (10) (1968) 1031–1055.
[42] É. Béchet, H. Minnebo, N. Moës, B. Burgardt, Improved implementation and robustness study of the X-FEM for stress analysis around cracks, Internat. J. Numer. Methods Engrg. 64 (8) (2005) 1033–1056.
[43] S. Osher, J.A. Sethian, Fronts propagating with curvature-dependent speed: algorithms based on Hamilton-Jacobi formulations, J. Comput. Phys. 79 (1) (1988) 12–49.
[44] N. Sukumar, D.L. Chopp, N. Moës, T. Belytschko, Modeling holes and inclusions by level sets in the extended finite-element method, Comput. Methods Appl. Mech. Engrg. 190 (46–47) (2001) 6183–6200.
[45] M.L. Williams, The bending stress distribution at the base of a stationary crack, J. Appl. Mech. 28 (1) (1961) 78–82.
[46] A.T. Zehnder, M.J. Viz, Fracture mechanics of thin plates and shells under combined membrane, bending, and twisting loads, Appl. Mech. Rev. 58 (1) (2005) 37–48.
[47] T. Chau-Dinh, G. Zi, P.-S. Lee, T. Rabczuk, J.-H. Song, Phantom-node method for shell models with arbitrary cracks, Comput. Struct. 92 (2012) 242–256.
[48] G. Nikishkov, S. Atluri, Calculation of fracture mechanics parameters for an arbitrary three-dimensional crack, by the 'equivalent domain integral' method, Internat. J. Numer. Methods Engrg. 24 (9) (1987) 1801–1821.
[49] N. Moës, A. Gravouil, T. Belytschko, Non-planar 3D crack growth by the extended finite element and level sets–Part I: Mechanical model, Internat. J. Numer. Methods Engrg. 53 (11) (2002) 2549–2568.
[50] T. Chau-Dinh, C. Mai-Van, G. Zi, T. Rabczuk, New kinematical constraints of cracked mitc4 shell elements based on the phantom-node method for fracture analysis, Eng. Fract. Mech. 199 (2018) 159–178.
[51] O. Zienkiewicz, J. Zhu, A simple error estimator and adaptive procedure for practical engineering analysis, Internat. J. Numer. Methods Engrg. 24 (2) (1987) 337–357.
[52] B. Brank, A. Ibrahimbegović, U. Bohinc, On discrete-Kirchhoff plate finite elements: Implementation and discretization error, in: Shell and Membrane Theories in Mechanics and Biology, Springer, 2015, pp. 109–131.
[53] W. Dörfler, A convergent adaptive algorithm for Poisson's equation, SIAM J. Numer. Anal. 33 (3) (1996) 1106–1124.
[54] A. Embar, J. Dolbow, I. Harari, Imposing Dirichlet boundary conditions with Nitsche's method and spline-based finite elements, Internat. J. Numer. Methods Engrg. 83 (7) (2010) 877–898.
[55] M.J. Viz, D.O. Potyondy, A.T. Zehnder, C.C. Rankin, E. Riks, Computation of membrane and bending stress intensity factors for thin, cracked plates, Int. J. Fract. 72 (1) (1995) 21–38.
[56] H.A. Sosa, J.W. Eischen, Computation of stress intensity factors for plate bending via a path-independent integral, Eng. Fract. Mech. 25 (4) (1986) 451–462.
[57] N. Nguyen-Thanh, W. Li, K. Zhou, Static and free-vibration analyses of cracks in thin-shell structures based on an isogeometric-meshfree coupling approach, Comput. Mech. (2018) 1–23.

[58] H. Zhang, J. Wu, D. Wang, Free vibration analysis of cracked thin plates by quasi-convex coupled isogeometric-meshfree method, Front. Struct. Civ. Eng. 9 (4) (2015) 405–419.
[59] B. Stahl, L. Keer, Vibration and stability of cracked rectangular plates, Int. J. Solids Struct. 8 (1) (1972) 69–91.
[60] C.L. Chan, C. Anitescu, T. Rabczuk, Isogeometric analysis with strong multipatch c1-coupling, Comput. Aided Geom. Design 62 (2018) 294–310.